Revision 1

Mesoproterozoic seafloor authigenic glauconite-berthierine: indicator of enhanced reverse weathering on early Earth

JIANBAI MA[1, 2], XIAOYING SHI[1, 2], MAXWELL LECHTE[4], XIQIANG ZHOU[5, 6], ZHENFEI WANG[7], KANGJUN HUANG[7], MAXIM RUDMIN[8], AND DONGJIE TANG*[1, 3]

[1]State Key Laboratory of Biogeology and Environmental Geology, China University of Geosciences (Beijing), Beijing 100083, China

[2]School of Earth Sciences and Resources, China University of Geosciences (Beijing), Beijing 100083, China

[3]Institute of Earth Sciences, China University of Geosciences (Beijing), Beijing 100083, China

[4]Department of Earth and Planetary Sciences, McGill University, 3450 University Street, Montréal, QC H3A 0E8, Canada

[5]Key Laboratory of Cenozoic Geology and Environment, Institute of Geology and Geophysics, Chinese Academy of Sciences, Beijing 100029, China

[6]College of Earth and Planetary Sciences, University of Chinese Academy of Sciences, Beijing 100049, China

[7]State Key Laboratory for Continental Dynamics and Early Life Institute, Department of Geology, Northwest University, Xi'an 710069, China

[8]Division for Geology, School of Earth Sciences & Engineering, Tomsk Polytechnic University, 634050 Tomsk, Russia

*Corresponding author. E-mail: dongjtang@126.com (D. Tang), Tel.: +86 10 82323199.

ABSTRACT

Sedimentary records suggest that the mid-Proterozoic (ca. 1.8–0.8 Ga) was persistently characterized by a greenhouse climate despite significantly lower solar luminosity compared to modern levels. To maintain greenhouse conditions, the partial pressure of carbon dioxide (pCO_2) must have remained elevated, possibly indicative of key differences in the complexities of the carbon cycle compared to the modern. Numerical modeling approaches have been used to suggest that high pCO_2 was likely maintained by elevated rates of 'reverse weathering': marine authigenic clay formation, a process that consumes alkalinity and generates CO_2. This process is kinetically slow in modern marine environments, yet is hypothesized to have been enhanced during the mid-Proterozoic due to the greater availability of important species for clay authigenesis such as silica and ferrous iron. This hypothesis is directly testable using the geological record, as enhanced reverse weathering would lead to the formation of abundant, marine authigenic clays. However, the distribution of marine authigenic clays in the Proterozoic sedimentary record has not been paid sufficient attention. In this study, we report the presence of authigenic clays (glauconite and berthierine) from the Xiamaling Formation (ca. 1.4 Ga), North China. The glauconite-berthierine horizons occur as millimeter- to centimeter-thick laminae interbedded with muddy siltstone, and feature detrital grains supported by the clay matrix. In places, these layers were partially reworked to form soft and cohesive intraclastic sands, suggesting a syndepositional origin. We hypothesize that marine iron cycling in the iron- and silica-rich mid-Proterozoic oceans may have facilitated authigenic iron-rich clay formation in the depositional basin of the Xiamaling Formation. The accumulation of iron-hydroxides on the seafloor—and the local increase in pH caused by subsequent dissimilatory iron reduction—could have resulted in the absorption of SiO_2, $Al(OH)_3$ and $Fe(OH)_2$ to form soft, cohesive and noncrystalline $Fe(OH)_3$-SiO_2-$Al(OH)_3$-$Fe(OH)_2$ gels. These gels would have subsequently converted to glauconite /

53 berthierine through ageing. The transformation from glauconite-rich layers to berthierine-rich
54 laminae was likely facilitated by a greater availability of Fe(II), and therefore higher
55 Fe(II)/TFe and Fe/Si ratios. We suggest that the relatively rapid formation of syndepositional,
56 seafloor berthierine and glauconite layers in the basal Xiamaling Formation is the result of
57 enhanced reverse weathering during this time. This study provides an important geological
58 support for carbon cycle models that invokes enhanced reverse weathering rates in the mid-
59 Proterozoic that may have helped to maintain a high baseline pCO_2 during this time.

60 **Keywords:** Ferruginous condition, dissimilatory iron reduction, Xiamaling Formation,
61 berthierine, glauconite, reverse weathering

62

63 ## INTRODUCTION

64 Solar luminosity has been consistently increasing through Earth's history, and was only
65 80–95% of modern levels throughout the Proterozoic Eon (2.5–0.54 Ga) (Gough 1981). Earth
66 system modeling shows that at this low solar radiation, global glaciation should be common
67 unless carbon dioxide (CO_2) was much higher than pre-industrial atmospheric levels (280
68 ppmv) (Kasting 1987; Sheldon 2006; Kanzaki and Murakami 2015; Fiorella and Sheldon
69 2017), even if other greenhouse gases such as methane (Pavlov et al. 2003; Kasting 2005;
70 Olson et al. 2016) and nitric oxide (Roberson et al. 2011; Stanton et al. 2018) were elevated.
71 However, the sedimentary record suggests that only a small fraction of the Proterozoic was
72 characterized by icehouse climate (Hambrey and Harland 1981; Chumakov and Elston 1989).

73 Geochronological constraints show that Neoproterozoic Era experienced two intensive
74 intervals of global glaciation during the Cryogenian Period—referred to as the Sturtian (ca.
75 720–660 Ma) and Marinoan (ca. 640–635 Ma) glaciations (e.g., Rooney et al. 2015; Zhou et
76 al. 2019)—as well as a comparatively short-lived ice age during the Ediacaran ca. 580 Ma
77 (e.g., De Alvarenga et al. 2007; Pu et al. 2016). The Paleoproterozoic Era also featured

multiple ice ages (e.g., Coleman 1907; Visser 1971; Hambrey and Harland 1981) that were dated to be the Siderian Period (2.50–2.30 Ga) (e.g., Caquineau et al. 2018; Warke et al. 2020). However, there are few, if any, unambiguously glacial deposits that have robust age constraints and were indicative of deposition in the mid-Proterozoic. Some glaciomarine sedimentary rocks have been suspected to be Tonian (1.00–0.72 Ga) (Hartley et al. 2020) and Stenian (1.2–1.0 Ga) (Geboy et al. 2013) in age, however, none of these is well-constrained in geochronology and globally distributed. Other possible geological evidence of glaciation has been used to argue for a glacial event in the Statherian Period (2.05–1.80 Ga) (Williams 2005; Kuipers and van der Wateren 2013), though this remains contentious. As such, glacial features are either absent or near-absent between the extreme ice ages of the Siderian and the Cryogenian, suggesting that a greenhouse climate was persistently maintained during the mid-Proterozoic.

Over geological timescales, atmospheric CO_2 levels are partly controlled by silicate weathering (Walker et al. 1981) and reverse weathering (e.g., Mackenzie and Garrels 1966; Isson and Planavsky 2018; Krissansen-Totton and Casting 2020). The weathering of silicates on continents and seafloor is a CO_2-consuming process (e.g., $CO_2 + 2H_2O + CaSiO_3 \rightarrow CaCO_3 + H_4SiO_4$); this reaction is temperature-dependent, which buffers the Earth's climate against increasing solar luminosity over time (Walker et al. 1981). In contrast, reverse weathering is a CO_2-producing process, and includes a variety of clay-forming reactions (i.e., amorphous Al silicate + cation + H_4SiO_4 + HCO_3^- → cation Al silicate + CO_2 + H_2O, or cation + H_4SiO_4 + HCO_3^- → cation silicate + CO_2 +H_2O). This process consumes alkalinity without carbon, thereby retaining CO_2 in the atmosphere-ocean system (Mackenzie and Kump 1995; Michalopoulos and Aller 1995; Isson and Planavsky 2018; Isson et al. 2020). Recently, geochemical and modeling studies have suggested that the sluggish kinetics of reverse weathering likely maintains an icehouse climate (e.g., Dunlea et al. 2017), while

enhanced reverse weathering would favor a greenhouse climate (Isson and Planavsky 2018; Isson et al. 2020; Krissansen-Totton and Catling 2020).

The authigenic formation of iron-rich clay minerals such as glauconite $[(K,Na)(Fe,Al,Mg)_2(Si,Al)_4O_{10}(OH)_2]$ and berthierine $[(Fe^{2+},Mg,Fe^{3+},Al)_3(Si,A1,Fe^{3+})_2O_5(OH)_4]$ may have been important reverse weathering processes in deep time. Glauconite is a phyllosilicate mineral of the dioctahedral mica group with 2:1 + interlayer ion structures (McRae 1972; Odin and Létolle 1980; Odin and Matter 1981; Banerjee et al. 2015, 2016). Authigenic glauconite precipitation ($0.55K^+ + 0.05Na^+ + 1.4Fe^{3+} + 0.2Fe^{2+} + 0.5Mg^{2+} + 3.8H_4SiO_4 + 0.2Al(OH)_3 + 6.2HCO_3^- \rightarrow K_{0.55}Na_{0.05}Fe^{3+}_{1.4}Mg_{0.5}Fe^{2+}_{0.2}Al_{0.2}Si_{3.8}O_{10}(OH)_2 + 6.2CO_2 + 10H_2O$) is interpreted to occur in marine environments with low clastic sedimentation rates (Amorosi 1995, 1997; Banerjee et al. 2015; Tang et al. 2017a), and is often associated with fecal pellets (e.g., Giresse and Odin, 1973). Berthierine is a dark green to brown iron-rich serpentine with a chemical composition similar to chamosite, but has a trioctahedral 1:1 layered silicate structure that has a basal spacing of 0.7 nm (serpentine group) (Brindley 1982; Bhattacharyya 1983; Hornibrook and Longstaffe 1996; Rivas-Sanchez et al. 2006). Berthierine (and its high temperature alteration product chamosite) is common in oolitic ironstones deposited in marginal marine environments (Kimberley 1979, 1980; Van Houten and Purucker 1984). Many Phanerozoic ironstones were deposited in shallow marine settings for which Fe(II) availability is interpreted to have been low (e.g., Maynard 1986; Cotter 1992). Therefore, the precipitation of berthierine ($2Fe^{2+} + H_4SiO_4 + 2Al(OH)_3 + 4HCO_3^- \rightarrow Fe_2Al_2SiO_5(OH)_4 + 4CO_2 + 5H_2O$) is generally considered to be a diagenetic process for these ironstones (e.g., Curtis and Spears 1968; Harder 1978; Taylor and Curtis 1995).

The authigenesis of berthierine and glauconite is kinetically slow in modern surface aqueous environments due to low concentrations of dissolved silica and iron. In contrast, the

128 authigenesis of these minerals may have been enhanced in Precambrian oceans, owing to
129 pervasive ferruginous (e.g., Canfield et al. 2008; Planavsky et al. 2011; Poulton and Canfield
130 2011; Tang et al. 2016, 2017a, 2017b, 2018, 2020; Lin et al. 2019) and Si-rich seawater
131 conditions (Maliva et al. 2005). In this context, a warm mid-Proterozoic climate could be
132 maintained even though solar luminosity was lower than today (Isson and Planavsky 2018;
133 Isson et al. 2020; Krissansen-Totton and Catling 2020). However, obtaining direct geological
134 evidence for an enhanced reverse weathering during the mid-Proterozoic is difficult largely
135 due to the low preservation potential of deep marine sediments on geological timescales, and
136 the fact that many authigenic clays are susceptible to post-deposition alteration. Isson and
137 Planavsky (2018) document sedimentary occurrences of authigenic, Fe-bearing clays such as
138 greenalite, minnesotaite and stilpnomelane throughout geological history. However, the
139 possibility that the authigenic formation of glauconite and berthierine on the seafloor (e.g.,
140 Tang et al. 2017b; Johnson et al. 2020) could have played an important role in reverse
141 weathering has not been fully explored. Here, we report layered glauconite and berthierine-
142 rich deposits from the ca. 1.4 Ga Xiamaling Formation, North China (Fig. 1), which features
143 textural evidence for enhanced reverse weathering during their deposition.
144

145 ## GEOLOGICAL SETTING

146 In North China, the Xiamaling Formation (~1.40–1.35 Ga) represents the last
147 sedimentary record before the final breakup of supercontinent Nuna (Columbia) (Zhao et al.
148 2003, 2004, 2011; Zhang et al. 2009, 2012b, 2017), which is marked by the widespread ~1.35
149 Ga diabase sills and ~1.33 Ga bimodal magmatic rocks shortly after the deposition of this
150 formation (Zhang et al. 2009, 2012a, 2015, 2017). The Xiamaling Formation is interpreted to
151 have been deposited in an extensional basin of the Yanliao Rift (Zhang et al. 2009, 2012b,
152 2017), although a back-arc setting has also been suggested based on a study of volcanic ash

beds in the formation (Meng et al. 2011). Paleogeographic studies indicate that this formation was deposited in an open marine setting, with the northern part of the Yanliao basin connected with the open ocean (Wang et al. 1985), although transient basin restriction may have existed (Diamond et al. 2018).

The Xiamaling Formation lies disconformably between the underlying Tieling Formation of Jixian Group and the overlying Changlongshan Formation of Qingbaikou Group (Fig. 2). The Xiamaling Formation is dominantly composed of dark shales and siltstone, which can be subdivided into four members (Member I to IV) in ascending order (Fig. 2; Tang et al. 2017b, 2018). These units are interpreted to have been deposited during a large transgressive-regressive cycle, with the black shales of Member III deposited during peak transgression (Fig. 2; Zhang et al. 2015, 2016; Tang et al. 2017b, 2018; Wang et al. 2017).

We studied the Xiamaling glauconite-berthierine precipitates near the Tielingzi village in Jixian (North China; Fig. 1). Only Member I outcrops at this locality (Fig. 3a). Member I is dominated by alternating reddish mudstone and green to gray muddy siltstone in the lowermost part (Fig. 3b–f), gray to black silty shale with abundant siderite concretions and siderite packstone bands in the lower part (Fig. 3g–l), and green silty shale in the middle to upper part (Fig. 3m). Storm influenced cross bedding, coarser-grained horizons of pebble conglomerates and quartz sandstone lenticles are common (Fig. 3f, i and l), indicative of a low-energy offshore transitional zone frequently influenced by storms. In other areas of North China, the lowermost part of this member is commonly characterized by purplish gravel-bearing sandstone (Tang et al. 2017b), particularly in the Zhaojiashan section (Hebei Province), which may represent lag deposits along a marine transgressive surface above the disconformity at the top of the Tieling Formation limestone. Glauconite-rich but berthierine-poor siltstones occur in the lowermost part of the member (Fig. 3b–f), while berthierine-rich

178 but glauconite-poor siltstones occur in the overlying layers (Fig. 3g–i).

179 Based on the zircon U-Pb ages of 1384.4 ± 1.4 and 1392.2 ± 1.0 Ma from the middle
180 Xiamaling Formation (Fig. 2; Zhang et al. 2015), and zircon and baddeleyite Pb-Pb ages of
181 1345 ± 12 and 1353 ± 14 Ma from diabase sills in the upper part (Zhang et al. 2009), the
182 duration of deposition of the Xiamaling Formation can be constrained between ~1.40 and
183 ~1.35 Ga (Tang et al. 2018). This formation unconformably overlies the Tieling Formation,
184 and is overlain by the Changlongshan Formation with a significant hiatus of *ca.* 400 Myr (Fig.
185 2; Gao et al. 2009; Tang et al. 2017b).

186 The Xiamaling Formation in most areas of North China is well preserved, and the
187 organic matter extracted from this formation are thermally immature to early thermally
188 mature, indicating a relatively low thermal evolution with burial temperatures of ≤90°C for
189 this formation (Luo et al. 2015; Zhang et al. 2015). In addition, a study of the Xiamaling
190 chamosite polytypes also suggests a burial depth of <2000 m, consistent with a burial
191 temperature of <80°C (Tang et al. 2017b). Paleomagnetic studies suggest that during the
192 deposition of the Xiamaling Formation, the North China Platform was located between 10°N
193 and 30°N (Evans and Mitchell 2011; Zhang et al. 2012b).

194

195 ## SAMPLES AND METHODS

196 Samples analyzed in this study were collected from the basal part of the Xiamaling
197 Formation at a freshly excavated quarry near Tielingzi village (40°05'22.30"N,
198 117°24"31.39"E), Jixian county, North China (Fig. 1). Collected samples were cut into chips
199 and only the fresh, central parts were used for mineralogical and geochemical analyses. For
200 geochemical analyses, fresh sample chips were cleaned, dried, and then glauconite-
201 berthierine-rich parts were drilled using a micro-drill with diamond bit.

202 Petrographic analysis was conducted on thin sections with a Stereo Discovery V20

203 microscope for large scope and a Zeiss Axio Scope A1 microscope for high magnification.
204 Ultra-structures were investigated on smoothed surface of chips using a Zeiss Supra 55 field
205 emission scanning electron microscope (FESEM) under 20 kV accelerating voltage with a
206 working distance of ~15 mm, in the FESEM Laboratory, China University of Geosciences
207 (Beijing). Secondary electron imaging detector was used to characterize topographic features,
208 and an AsB detector was used to reveal compositional difference (backscattered electron,
209 BSE, image). Samples were coated with 8 nm thick carbon for electric conduction before
210 analysis. Smooth sample surfaces for electron microscopy were further polished using ion
211 milling with GATAN Ilion 697 ion mills. Element concentrations of micron-sized spots were
212 quantitatively analyzed by an Oxford energy-dispersive X-ray spectrometer (EDS) connected
213 to the FESEM, operated at 20 kV with a working distance of ~15 mm and beam diameter of
214 ~2 μm (Tang et al. 2017b, 2020). Duplicate analyses of individual points showed analytical
215 error of less than 3%. The mineralogy was determined by electron backscatter diffraction
216 (EBSD) using a Zeiss Supra 55 FESEM equipped with an Oxford NordlysNano EBSD
217 acquisition camera following the method described in Tang et al. (2020). Only measurements
218 with mean angular deviation (MAD) values below 1.0° were accepted for analyses, and the
219 indexing rate is about 80%.

220 Sixteen purified glauconite- or berthierine-rich powder samples were chosen for X-ray
221 diffraction (XRD) analysis. Purified clay mineral samples were separated from 200-mesh
222 bulk rock powder through sedimentation and centrifuge. The purified random samples were
223 scanned after air-drying, using nickel filter copper radiation in a SmartLab X-Ray
224 Diffractometer at China University of Geosciences (Beijing) following the methods described
225 in Tang et al. (2017b). Four representative samples were selected for Transmission Electron
226 Microscopy (TEM) observation to identify the interstratification of different iron-bearing clay
227 minerals at China University of Geosciences (Beijing). The procedure of sample preparation

followed that described in Tang et al. (2017b). The sample powder on the copper mesh was analyzed using a Hitachi H-8100 TEM, equipped with a tungsten filament electron source (operated at 200 kV), and an EDAX X-ray analyzer with an ultrathin window.

For major element analysis, the same purified powder samples as those for the XRD analysis were used. About 50 mg sample powder was dissolved in 250 mg lithium metaborate at 990 °C for 20 min and then diluted to 100 ml by 18.25 MΩ Milli-Q water before element measurement using Inductively Coupled Plasma Optical Emission Spectrometry (ICP-OES) at China University of Geosciences (Beijing). Fe(II)/Fe(III) ratio of samples was determined by ICP-OES and classical titration technique. In this method, $HF/H_4SO_4/H_3BO_3$ was used to dissolve samples, $K_2Cr_2O_7$ was used to titrate the solution, and sodium diphenylamine sulfonate solution was used as color indicator. The accuracy of all ICP-OES analyses is better than 5% (relative) for analyzed elements. Trace element analyses of clay minerals were conducted at the National Research Center of Geoanalysis in Beijing, following the method described in Zhou et al. (2018) using a LA-ICP-MS. The accuracy of LA-ICP-MS analysis is better than 10% (relative) for the analyzed elements. Cerium (Ce) anomalies were calculated using the equation $Ce_{SN}/Ce_{SN}^* = Ce_{SN}/(Pr_{SN}^2/Nd_{SN})$ as suggested by Lawrence et al. (2006) in order to avoid the potential influence of positive La anomalies; where the subscript SN represents REE normalized by PAAS (Post-Archean Australian Shale). Europium (Eu) anomalies were calculated as $Eu_{SN}/Eu_{SN}^* = Eu_{SN}/(0.66Sm_{SN} + 0.33Tb_{SN})$ in order to avoid the potential influence from the seawater positive Gd anomaly (Planavsky et al. 2010).

RESULTS

Two types of iron clay-rich rocks were identified in the studied interval: (1) glauconite-rich muddy siltstone (Fig. 4a and b) and (2) berthierine-rich muddy siltstone (Fig. 4c and d). Glauconite-rich muddy siltstone is yellow-green to brown in color (Fig. 4a and b). These

253 siltstones contain horizons of pebble- and sand-sized glauconite grains (Fig. 3f). The
254 association of these pebble and sand-sized glauconite grains with the underlying glauconite-
255 rich siltstone laminae suggests that these glauconite grains are intraclastic in origin, which
256 likely formed during storm events (Fig. 4a and b). The berthierine-rich muddy siltstones are
257 gray in color and feature alternating muddy and silty laminae (Fig. 4c and d)—which can be
258 cross-laminated (Fig. 4e)—with berthierine being more abundant in the silty laminae. Siderite
259 concretions that deflect siltstone laminae are common (Fig. 4f), with larger siderite nodules
260 (Fig. 4g) and beds predominantly composed of siderite sands (Fig. 4h) becoming more
261 abundant in the overlying interval of Member I.

262 The results of XRD analysis shows that gray and green siltstones have similar
263 mineralogical compositions, but varying in their relative abundance of iron-bearing clays.
264 The air-dried samples exhibit strong reflections of (002) and (004) at 0.710 (12.50°) and
265 0.355 nm (25.18°), and relatively weak reflections of (001), (003) and (005) at 1.420 (6.24°),
266 0.472 (18.86°), and 0.284 nm (31.60°), respectively, indicating the presence of chamosite.
267 The reflection of (100) at 0.467 nm (19.04°) suggests the presence of berthierine (Fig. 5a;
268 Kozłowska and Maliszewska 2015). The wide (005) peak at 2.840 nm (31.48°) but narrow
269 (004) peak at 0.354 nm (25.20°) suggests that a large amount of berthierine is preserved and
270 has not been transformed into chamosite (Fig. 5a; Ryan and Reynolds Jr. 1996; Tang et al.
271 2017b). The intense basal reflection (001) at 1.00 nm *d*-spacing (8.86°) and weak basal
272 reflections (003) at 0.33 nm (26.68°), (004) at 0.25 nm (35.84°) and (005) at 0.20 nm *d*-
273 spacing (45.42°) are the characteristic peaks of glauconite (Fig. 5a; Tang et al. 2016). The
274 occurrences of berthierine (Fig. 5b), interstratification of berthierine and chamosite (Fig. 5c),
275 glauconite (Fig. 5d), and interstratification of glauconite and chamosite (Fig. 5e) are also
276 confirmed by TEM observations.

277 The glauconite-rich layers within the Xiamaling Formation siltstones are commonly

several centimeters in thickness and feature isolated detrital grains within the glauconite matrix (Fig. 6a–c). The berthierine-rich laminae are thinner (typically 0.5–2 mm; Fig. 6d and e), and contain coarser detrital grains than those in adjacent muddy laminae (Fig. 6d and e). Under high magnification, the berthierine structure can be observed as radiating fans resembling a "bowtie". These berthierine “bowties” are randomly distributed and closely interwoven with each other (Fig. 6f). Berthierine intraclasts can also be observed (Fig. 6g): in places, these have undergone soft sediment deformation (Fig. 6h). Berthierine-poor, muddy laminae penetrate into berthierine-rich layers as flame structures (Fig. 6i). In the berthierine-rich laminae, detrital grains (commonly quartz, feldspar and mica) are supported by the berthierine matrix (Figs. 6j–l and 7), including some grains oriented with subvertical long axes (Fig. 6k). These detrital grains are well preserved without obvious re-dissolution or replacement textures (Fig. 6l). Hematite relics are rare in the berthierine-rich or glauconite-rich siltstones, but can be observed occasionally in siderite concretions (Fig. 6m–o).

The major element contents of green and gray muddy siltstone are shown in Table S1. The total Fe oxide (TFe_2O_3) contents are similar for the green (22.30 ± 5.52 wt%; n = 9) and gray muddy siltstones (22.70 ± 2.27 wt%; n = 7); however, the Fe(II)/TFe ratios are distinct (0.44 ± 0.11 and 0.74 ± 0.10 respectively). It is difficult to precisely determine the chemical composition of the berthierine or glauconite in the Xiamaling Formation, because they are commonly interstratified on the nanometer scale (Fig. 5). Based on the quantitative EDS analytical results (Table S2), however, the berthierine and glauconite endmembers can be identified (Fig. 8a–d). The berthierine endmember comprises 37–44 wt% TFe_2O_3, 25–30 wt% SiO_2, 4–7 wt% MgO, and 21–26 wt% Al_2O_3 with negligible content of K_2O, while the glauconite endmember consists of lower TFe_2O_3, higher SiO_2 and K_2O, and similar MgO and Al_2O_3. The glauconite-berthierine samples (n = 11) have total rare earth element (ΣREE) contents of 38–372 μg/g. The $Pr_{(SN)}/Yb_{(SN)}$ ratios are typically of 0.70 ± 0.31 for the

glauconite-berthierine, indicative of a minor depletion in the light REEs (Fig. 8e and f, Table S3). These samples commonly show positive Ce anomalies ($Ce_{SN}/Ce_{SN}^* \leq 1.67$; see Methods for formulae), and lack Eu anomalies (average $Eu_{SN}/Eu_{SN}^* = 0.99 \pm 0.20$; Table S3). The Xiamaling Formation glauconite and berthierine are of low Y/Ho ratios (average Y/Ho = 25) compared to modern seawater (Y/Ho > 44; Bau 1996).

DISCUSSION

Textural evidence for marine reverse weathering

The fine lamination of glauconite and berthierine in the Xiamaling Formation siltstones (Figs. 3e, f, h, i, 6d and e) suggests that they were formed essentially at the sediment–seawater interface with a primary to very early diagenetic origin. Fine lamination can also be preserved in early diagenetic nodules, either due to replacement of preexisting clastic laminae or due to displacive crystallization forcing apart sedimentary beds below the sediment–seawater interface (cf. Gaines and Vorhies 2016; Liu et al. 2019). However, the extensive reworking and soft deformation observed in glauconite-berthierine layers (Fig. 6g–i), and the intraclastic glauconite-berthierine pebble-bearing sands (Figs. 4a, b, 6g and h), are supportive of the formation of glauconite and berthierine either on the seafloor or near the sediment–seawater interface prior to significant burial compaction. Flame and ball-and-pillow structures observed at the boundary between berthierine layers and underlying mudstone laminae (Fig. 6i) also support the interpretation that the berthierine beds were likely deposited prior to burial and compaction. Isolated detrital grains suspended within the glauconite and berthierine matrix (Figs. 6a–c, j–l and 7)—including grains with apparently unstable orientations (Fig. 6k)—likely indicate that the detrital particles were deposited on pre-existing, unsolidified glauconite/berthierine layers on seafloor. The presence of randomly distributed and interwoven, radiating fans of "bowtie" berthierine in the berthierine laminae

328 (Fig. 6f) is supportive of an authigenic origin for the berthierine, and suggests crystallization
329 of berthierine from precursor gels. Thus, both the sedimentological and petrographic features
330 of the ferrous clay-rich strata of the Xiamaling Formation support the interpretation that the
331 glauconite and berthierine layers formed authigenically at the sediment–seawater interface.
332
333 **Insights from modern and Phanerozoic berthierine and glauconite**
334 Modern glauconite commonly forms in relatively deep marine settings (i.e., greater than
335 50 m water depth) (Odin and Matter 1981; Logvinenko 1982; Odin 1988), and middle to
336 outer shelf settings (~50–500 m depth) are the most favorable depositional environments
337 suggested for Phanerozoic glauconite (Odin and Matter 1981; Banerjee et al. 2016). These
338 glauconite deposits are typically present as peloids (typically interpreted as fecal pellets) or as
339 infills in the voids within bioclasts (Giresse and Odin 1973; Odin and Matter 1981;
340 Baldermann et al. 2012; Banerjee et al. 2016). These porous substrates are considered to
341 favor glauconite authigenesis by facilitating ferruginous conditions in porewaters, possibly
342 coupled with the degradation of organic matter (Meunier and El Albani 2007; Baldermann et
343 al. 2012).
344 In geological record, berthierine is most obviously represented by Phanerozoic ironstone
345 deposits (Young 1989), which are often considered to be formed during stratigraphic
346 condensation (Bhattacharyya 1983; Bayer 1989). However, berthierine authigenesis is rare to
347 absent in modern marine environments (Odin 1988), with a possible example of peloidal
348 berthierine documented in a temperate basin in Scotland (Rohrlich et al. 1969). More
349 commonly reported from Holocene marine environments is odinite (Bailey 1988), a kind of
350 dioctahedral-trioctahedral clay similar to berthierine that is typically Fe(III)-rich, and some
351 deposits of ancient berthierine have been suggested to be formed via the diagenetic
352 replacement of odinite (Odin 1988; Velde 1995). Odinite formation is largely restricted to

353 tropical, estuarine mud banks (e.g., Porrenga 1967; Giresse and Odin 1973) with an abundant
354 supply of continental iron (Aller et al. 1986). As with most glauconite deposits, Holocene
355 odinite is near-exclusively infilling porous grains or skeletal fragments, or associated with
356 fecal pellets (Bailey 1988; Odin 1988; Hornibrook and Longstaffe 1996). In sum, it appears
357 that warm seawater, reducing conditions and active iron cycling have facilitated the
358 authigenesis of Fe-rich clays such as glauconite, odinite and berthierine.
359

360 **Mechanisms for berthierine and glauconite authigenesis**

361 The pathway of berthierine formation in sedimentary environments remains contentious.
362 Several possible pathways for its formation have been proposed (Harder 1978; Bhattacharyya
363 and Kakimoto, 1982; Iijima and Matsumoto 1982; Bhattacharyya 1983; Odin 1988; Mücke
364 2006; Fu et al. 2015; Tang et al. 2017b), including: (1) crystallization from noncrystalline
365 precursor gels (such as SiO_2-$Al(OH)_3$-$Fe(OH)_3$ precipitates) under reducing conditions, (2)
366 transformation from kaolinite, odinite or glauconite, (3) dissolution of argillaceous sediments
367 and reprecipitation, and (4) replacement of calcareous oolites. Glauconite is suggested to
368 form through the transformation pre-existing clay minerals, the replacement of feldspar
369 during early digenesis, or precipitate as an authigenic phase (e.g., Banerjee et al. 2015, 2016;
370 Tang et al. 2017a). In this study, the preservation of detrital minerals including illite, mica,
371 feldspar and quartz without obvious dissolution features (Fig. 6l) suggests that the majority of
372 the Xiamaling berthierine and glauconite was not directly transformed from detrital clay
373 minerals. Further, we see no evidence for the partial transformation of precursor minerals into
374 glauconite or berthierine in the Xiamaling Formation, although glauconite could transform
375 into berthierine (Tang et al. 2017b). In addition, primary carbonates have not been observed
376 in the Member I of the Xiamaling Formation, implying that the berthierine is unlikely formed
377 through replacement of carbonate minerals. Therefore, we suggest that the glauconite and

berthierine-rich strata in the Xiamaling Formation formed due to the early diagenetic crystallization of a primary Fe-rich gel (such as noncrystalline $Fe(OH)_3$-SiO_2-$Al(OH)_3$-$Fe(OH)_2$) generated under reducing conditions at the sediment–seawater interface.

In this scenario, the requisite elements could be supplied by iron cycling (in both the water column and sediment pile). The rapid dissolution and transformation of smectite to illite by microbial dissimilatory reduction is the most likely process to provide sufficient Al for the formation of other authigenic clay minerals (cf. Kim et al. 2004; Hodgskiss et al. 2018). Laboratory experiments have proved that this is a rapid process with 43% smectite being converted to illite within 14 days (Kim et al. 2004). The formation of Fe-bearing clay minerals requires the availability of Fe(II), which enables an octahedral layer of the brucite-gibbsite type to be formed, and is necessary for the bidimensional orientation of SiO_4-tetrahedra leading to clay mineral formation (Harder 1978). Because Fe(II) is readily oxidized to Fe(III) under oxic conditions (forming Fe(III) hydroxide-silica gels that age to goethite, hematite and quartz; e.g., Harder and Flehmig 1970), the formation of Fe-rich clays such as berthierine and glauconite requires anoxic–suboxic conditions (e.g., Curtis 1985; Van Houten and Purucker 1985; Glenn and Arthur 1988; Taylor 1990). Fe(II) at the sediment–seawater interface may be supplied from benthic porewater flux (supplied from the local reduction of ferric minerals in the underlying sediment pile), or from upwelling ferruginous seawater enriched in Fe(II) from distal sources such as hydrothermal fluids. Importantly, the lack of iron-rich detrital minerals or their relics, such as hematite and biotite, in the associated strata suggests that redox cycling of direct continental Fe(III) input is not the major source of Fe(II) for the glauconite and berthierine deposits of the Xiamaling Formation. However, deep marine waters are considered to have been dominantly ferruginous during the mid-Proterozoic (Planavsky et al. 2011). The impinging of ferruginous waters onto the shallow shelf was likely a common process during the deposition of the lower Xiamaling Formation.

This process is interpreted to have facilitated the transformation of glauconite to chamosite in the lower Member II of the Xiamaling Formation (Tang et al. 2017), and led to the formation of siderite iron formation in the lower Member II (Canfield et al. 2018; Tang et al. 2018). Ferruginous seawater may have also led to the deposition of marine red beds in the middle Member II (Tang et al. 2020). Therefore, we suggest that the wide presence of glauconite and berthierine in the Xiamaling Formation implies that ferruginous waters impinged onto the shallow shelf in North China during the deposition of Member I. Vigorous iron cycling near the basinal redoxcline may have facilitated the authigenesis of glauconite and berthierine-rich strata.

We suggest that the formation of the berthierine gel precursor during the Xiamaling deposition was favored by ferruginous conditions near the sediment–seawater interface. Previous studies indicate that higher pH and more negative Eh values are more favorable for and lead to a better crystallization of authigenic iron-bearing clays in shorter times (Harder 1978; Baldermann et al. 2013; Francisco et al. 2020). Di- and tri-octahedral iron clay minerals were preferably formed from solutions with elevated pH over 7, mostly between 8 and 9 (Harder 1978; Rasmussen et al. 2017; Francisco et al. 2020). In addition, adsorption of Si onto Fe and Al oxides increases with increasing pH, and reaches a maximum at pH 9 (Hingston and Raupach 1967; Huang 1975; Sigg and Stumm 1981). The anoxic bottom waters in the Yanliao Basin would also favor dissimilatory iron reduction [$4Fe(OH)_3 + CH_2O \rightarrow FeCO_3 + 3Fe^{2+} + 6OH^- + 4H_2O$], therefore increasing the micro-environmental pH and supplying Fe(II), which is also consistent with the early diagenetic origin of siderite in the berthierine-bearing layers (Fig. 4f; Tang et al. 2018). The supply of ferrihydrite to the seafloor due to the oxidation of Fe(II) in upwelling ferruginous seawater, coupled with reducing bottom waters and elevated pH, could lead to the generation of sufficient SiO_2-$Al(OH)_3$-$Fe(OH)_2$ to form gels, which could subsequently be transformed to berthierine

during ageing (Fig. 9).

The Fe(II)/TFe ratios in glauconite-rich or berthierine-rich muddy siltstones are lower than unity (1/1) but hematite is rare in these muddy siltstones, implying that large amount of Fe(II) was oxidized around the redoxcline in shallower seawater, then precipitated as ferrihydrite in the water column, which was subsequently reduced (likely via dissimilatory iron reduction) and incorporated into ferrous phases such as glauconite and/or berthierine. This explanation is consistent with evidence for a weakly oxygenated surface seawater during the time, as supported by the positive Ce anomaly in glauconite-berthierine precipitates. In an oxic water column, Ce is preferably removed by Mn–oxyhydroxides (e.g., German and Elderfield 1990; Bau and Dulski 1999; Haley et al. 2004; Gutjahr et al. 2007; Planavsky et al. 2010). The Ce absorbed or scavenged to Mn–oxyhydroxides can be subsequently released below the Mn redoxcline, positive Ce anomalies will be resulted in the chemical sediments precipitated at or near this redoxcline (e.g., de Baar et al. 1988; German et al. 1991; Bau et al. 1997; De Carlo and Green 2002; Planavsky et al. 2010). Thus, the presence of positive Ce anomaly likely reflects active Mn redox cycling in the water column and porewaters, which has been recorded by the authigenic glauconite-berthierine (cf. Liu et al. 2019).

We suggest that the glauconite of the Xiamaling Formation likely formed through a similar pathway as that of berthierine but under higher Eh, as berthierine and glauconite are intimately associated in Member I. The alternation between glauconite and berthierine authigenesis is likely controlled by the Si/Fe and Fe(II)/TFe ratios in the noncrystalline precursor of $Fe(OH)_3$-SiO_2-$Al(OH)_3$-$Fe(OH)_2$ gel. Very low Si/Fe ratio in the precipitates would inhibit clay mineral formation (Harder 1978). High Si/Fe molar ratios (i.e., ~3:1 to 10:1) would facilitate the formation of three-layer clay minerals such as nontronite or glauconite, whereas moderately Si/Fe molar ratios (i.e., ~1:2 to 2:1) favor the formation of two-layer clay minerals such as greenalite and berthierine, at low temperature (Harder 1978;

453 Tosca et al. 2016; Francisco et al. 2020). The elevated flux of Fe(II) from ferruginous
454 seawater to shallow settings would result in the accumulation of more total iron in the gels
455 and the formation of more reducing seawater conditions above storm wave base. These
456 processes would, in turn, lead to lower Si/Fe but higher Fe(II)/TFe ratios, thus favoring the
457 formation of berthierine over glauconite (Fig. 9).
458
459 **IMPLICATIONS**
460 Authigenic formation of glauconite and berthierine are two common reverse weathering
461 (CO_2 producing) processes that were likely more favorable in Precambrian oceans due to the
462 higher availability of marine silica and ferrous iron (Isson and Planavsky 2018). In modern
463 oceans, glauconite authigenesis is typically a slow process, and commonly requires 0.1–1
464 Myr for the formation of highly evolved glauconite (Odin and Létolle 1980; Baldermann et al.
465 2013), and evolved glauconitic horizons in the Phanerozoic stratigraphic record are often
466 associated with condensed sections (Banerjee et al. 2016). The formation of berthierine is
467 considered to largely take place in ferruginous porewater (Taylor 1990), because this process
468 is inhibited in oxic bottom waters (Harder 1978). However, the emerging consensus that the
469 Proterozoic was characterized by dominantly ferruginous oceans (e.g., Sperling et al. 2015)
470 presents the intriguing possibility that authigenic Fe-bearing clay formation was rapid and
471 facilitated by Fe(II)- and Si-rich seawater conditions (Isson and Planavsky 2018).
472 Petrographic evidence shows that the formation of glauconite in mid-Proterozoic oceans
473 could be a comparatively rapid process. For instance, highly evolved glauconite formed in
474 environment with high precipitation rates has been reported from the stromatolite reefs of the
475 Mesoproterozoic Tieling Formation (Tang et al. 2017a), and is also supported by the
476 petrographic and sedimentological evidence for the rapid accumulation of authigenic
477 glauconite layers on the seafloor in this study. It seems that the formation of syndepositional

478 berthierine was likely also a fast process in the ferruginous mid-Proterozoic oceans (Johnson
479 et al. 2020).

480 In mid-Proterozoic shallow seawater, the relatively rapid formation of iron-bearing clay
481 minerals (such as glauconite and berthierine) through reverse weathering was likely a
482 common phenomenon as documented by well-preserved examples in North China (Tang et al.
483 2017a, 2017b) and the Roper Basin (north Australia) (Johnson et al. 2020). The formation of
484 greenalite (e.g., Rasmussen et al. 2017; Isson and Planavsky 2018; Johnson et al. 2020;
485 Muhling and Rasmussen 2020), stilpnomelane and minnesotaite (Isson and Planavsky 2018)
486 has also been widely documented in mid-Proterozoic marine deposits. Therefore, there is a
487 growing body of geological evidence that supports extensive reverse weathering in the mid-
488 Proterozoic oceans. We suggest that the geological distribution of berthierine and glauconite
489 in Precambrian strata should be reassessed in light of its potential evidence for reverse
490 weathering.

491 It is difficult to give a precise estimation on the amount of authigenic glauconite and
492 berthierine that was deposited in the Yanliao basin, because the real volume of the original
493 Xiamaling deposits and the preserved proportion in relative to this sedimentary succession
494 are not know at present. Assuming that the glauconite and berthierine were precipitated in the
495 whole area of 60,000 km^2 as the Xiamaling Formation distribution (cf. Canfield et al. 2018)
496 with a total thickness of 1 m, a total product of 160 Gt glauconite or 182 Gt berthierine could
497 be estimated. With such a huge amount of glauconite or berthierine precipitates, the amount
498 of CO_2 produced in this process would be approximately 14 ppmv or 13 ppmv CO_2
499 respectively (i.e., approximately 5% of pre-industry levels). In fact, the glauconite-berthierine
500 deposits observed in the Xiamaling Formation possibly extend for at least 200 km across the
501 North China Platform (from Jixian section to Huailai section) (Tang et al., 2017b). This
502 would imply that the Xiamaling glauconite-berthierine was substantial at its original

503 deposition. Therefore, we think that the estimated glauconite-berthierine precipitation is
504 likely in the right order of magnitude.

505 Given that the early ocean was likely ferruginous and Si-rich for much of the mid-
506 Proterozoic history (e.g., Planavsky et al. 2011; Poulton and Canfield 2011; Sperling et al.
507 2015), the authigenic formation of berthierine, glauconite and other clay minerals may have
508 played an important role in maintaining a high baseline pCO_2 and keeping a warm climate
509 during the time (Isson and Planavsky 2018). Although the glauconite and berthierine-rich
510 strata of the Xiamaling Formation represent only a local record of authigenic clay formation
511 in the mid-Proterozoic, and their potential impacts on the global carbon cycle are difficult to
512 assess, this study supports the hypotheses of enhanced reverse weathering during this time
513 (e.g., Isson and Planavsky 2018). We think that as more research into the geological records
514 of authigenic Fe-rich clays, the possible influence of enhanced reverse-weathering on the
515 climate during Precambrian could be elucidated in a more quantitative way.

516

517 **ACKNOWLEDGMENTS**

518 The study was supported by the National Natural Science Foundation of China (Nos.
519 41930320, 41972028, 41973008), the Key Research Program of the Institute of Geology &
520 Geophysics, CAS (No. IGGCAS-201905), the Chinese "111" project (B20011), and by the
521 Fundamental Research Funds for the Central Universities (Nos. 2652019093, 265201925).
522 Maxwell Lechte acknowledges funding from the Fonds de Recherche du Québec—Nature et
523 Technologies. Thanks are also given to Yong Han for her kind help in TEM analysis, and
524 Mohan Shang, Yang Li, Haoming Wei and Zhipeng Wang for their assistance in fieldwork.

525

526 **REFERENCES CITED**

527 Aller R.C., Mackin J.E., and Cox R.T. Jr. (1986) Diagenesis of Fe and S in Amazon inner

shelf muds: apparent dominance of Fe reduction and implications for the genesis of ironstones. Continental Shelf Research, 6, 263–289.

Amorosi, A. (1995) Glaucony and sequence stratigraphy; a conceptual framework of distribution in siliciclastic sequences. Journal of Sedimentary Research, 65, 419–425.

——— (1997) Detecting compositional, spatial, and temporal attributes of glaucony: a tool for provenance research. Sedimentary Geology, 109, 135–153.

Bailey, S.W. (1988) Odinite, a new dioctahedral-trioctahedral Fe^{3+}-rich 1:1 clay mineral. Clay Miner, 23, 237–247.

Baldermann, A., Grathoff, G.H., and Nickel, C. (2012) Micromilieu-controlled glauconitization in fecal pellets at Oker (Central Germany). Clay Minerals, 47, 513–538.

Baldermann, A., Warr, L.N., Grathoff, G.H., and Dietzel, M. (2013) The rate and mechanism of deep-sea glauconite formation at the Ivory Coast–Ghana Marginal Ridge. Clays and Clay Minerals, 61, 258–276.

Banerjee, S., Mondal, S., Chakraborty, P.P., and Meena, S.S. (2015) Distinctive compositional characteristics and evolutionary trend of Precambrian glaucony: example from Bhalukona Formation, Chhattisgarh basin, India. Precambrian Research, 271, 33–48.

Banerjee, S., Bansal, U., and Thorat, A.V. (2016) A review on palaeogeographic implications and temporal variation in glaucony composition. Journal of Palaeogeography, 5, 43–71.

Bau, M. (1996) Controls on the fractionation of isovalent trace elements in magmatic and aqueous systems: evidence from Y/Ho, Zr/Hf, and lanthanide tetrad effect. Contributions to Mineralogy and Petrology, 123, 323–333.

Bau, M., and Dulski, P. (1999) Comparing yttrium and rare earths in hydrothermal fluids from the Mid-Atlantic Ridge: implications for Y and REE behaviour during near-vent mixing and for the Y/Ho ratio of Proterozoic seawater. Chemical Geology, 155, 77–90.

553 Bau, M., Möller, P., and Dulski, P. (1997) Yttrium and lanthanides in eastern Mediterranean
554 seawater and their fractionation during redox-cycling. Marine Chemistry, 56, 123–131.
555 Bayer, U. (1989) Stratigraphic and environmental patterns of ironstone deposits. Geological
556 Society, London, Special Publications, 46, 105–117.
557 Bhattacharyya, D.P. (1983) Origin of berthierine in ironstones. Clays and Clay Minerals, 31,
558 173–182.
559 Bhattacharyya, D.P., and Kakimoto, P.K. (1982) Origin of ferriferous ooids: an SEM study of
560 ironstone ooids and bauxite pisoids. Journal of Sedimentary Research, 52, 849–857.
561 Brindley, G.W. (1982) Chemical compositions of berthierines—A review. Clays and clay
562 Minerals, 30, 153–155.
563 Canfield, D.E., Poulton, S.W., Knoll, A.H., Narbonne, G.M., Ross, G., Goldberg, T., and
564 Strauss, H. (2008) Ferruginous conditions dominated later Neoproterozoic deepwater
565 chemistry. Science, 321, 949–952.
566 Canfield, D.E., Zhang, S.C., Wang, H.J., Wang, X.M., Zhao, W.Z., Su, J., Bjerrum, C.J.,
567 Haxen, E.R., and Hammarlund, E.U. (2018) A Mesoproterozoic iron formation.
568 Proceedings of the National Academy of Sciences of the United States of America, 115,
569 E3895–E3904.
570 Caquineau, T., Paquette, J.L., and Philippot, P. (2018) U-Pb detrital zircon geochronology of
571 the Turee Creek Group, Hamersley Basin, Western Australia: timing and correlation of
572 the Paleoproterozoic glaciations. Precambrian Research, 307, 34–50.
573 Chumakov, N.M., and Elston, D.P. (1989) The paradox of Late Proterozoic glaciations at low
574 latitudes. Episodes Journal of International Geoscience, 12, 115–120.Cotter, E. (1992)
575 Diagenetic alteration of chamositic clay minerals to ferric oxide in oolitic ironstone.
576 Journal of Sedimentary Research, 62, 54–60.
577 Coleman, A.P. (1907) A lower Huronian ice age. American Journal of Science, 23, 187–192.

578 Curtis, C.D. (1985) Clay mineral precipitation and transformation during burial diagenesis.
579 Philosophical Transactions of the Royal Society of London, Series A, Mathematical and
580 Physical Sciences, 315, 91–105.
581 Curtis, C.D., and Spears, D.A. (1968) The formation of sedimentary iron minerals. Economic
582 Geology, 63, 257–270.
583 De Alvarenga, C.J.S., Figueiredo, M.F., Babinski, M., and Pinho, F.E.C. (2007) Glacial
584 diamictites of Serra Azul Formation (Ediacaran, Paraguay belt): evidence of the
585 Gaskiers glacial event in Brazil. Journal of South American Earth Sciences, 23, 236–241.
586 De Baar, H.J.W., German, C.R., Elderfield, H., and Van Gaans, P. (1988) Rare earth element
587 distributions in anoxic waters of the Cariaco Trench. Geochimica et Cosmochimica Acta,
588 52, 1203–1219.
589 De Carlo, E.H., and Green, W.J. (2002) Rare earth elements in the water column of Lake
590 Vanda, McMurdo Dry Valleys, Antarctica. Geochimica et Cosmochimica Acta, 66,
591 1323–1333.
592 Diamond, C.W., Planavsky, N.J., Wang, C., and Lyons, T.W. (2018) What the ~1.4 Ga
593 Xiamaling Formation can and cannot tell us about the mid-Proterozoic ocean.
594 Geobiology, 16, 219–236.
595 Dunlea, A.G., Murray, R.W., Ramos, D.P.S., and Higgins, J.A. (2017) Cenozoic global
596 cooling and increased seawater Mg/Ca via reduced reverse weathering. Nature
597 Communications, 8, 1–7.
598 Evans, D.A.D., and Mitchell, R.N. (2011) Assembly and breakup of the core of
599 Paleoproterozoic–Mesoproterozoic supercontinent Nuna. Geology, 39, 443–446.
600 Fiorella, R.P. and Sheldon, N.D. (2017) Equable end Mesoproterozoic climate in the absence
601 of high CO_2. Geology, 45, 231–234.
602 Francisco, P.C.M., Mitsui, S., Ishidera, T., Tachi, Y., Doi, R., and Shiwaku, H. (2020)

Interaction of Fe^{II} and Si under anoxic and reducing conditions: Structural characteristics of ferrous silicate co-precipitates. Geochimica et Cosmochimica Acta, 270, 1–20.

Fu, Y., Van Berk, W., Schulz, H.M., and Mu, N. (2015) Berthierine formation in reservoir rocks from the Siri oilfield (Danish North Sea) as result of fluid–rock interactions: Part II. Deciphering organic–inorganic processes by hydrogeochemical modeling. Marine and Petroleum Geology, 65, 317–326.

Gaines, R.R., and Vorhies, J.S. (2016) Growth mechanisms and geochemistry of carbonate concretions from the Cambrian Wheeler Formation (Utah, USA). Sedimentology, 63, 662–698.

Gao, L.Z. Zhang, C.H., Liu, P.J., Ding, X.Z., Wang, Z.Q., and Zhang, Y.J. (2009) Recognition of Meso- and Neoproterozoic stratigraphic framework in North and South China. Acta Geoscientica Sinica, 30, 433–466 (in Chinese with English abstract).

Geboy, N.J., Kaufman, A.J., Walker, R.J., Misi, A., de Oliviera, T.F., Miller, K.E., Azmy, K., Kendall, B., and Poulton, S.W. (2013) Re–Os age constraints and new observations of Proterozoic glacial deposits in the Vazante Group, Brazil. Precambrian Research, 238, 199–213.

Glenn, C.R., and Arthur, M.A. (1988) Petrology and major element geochemistry of Peru margin phosphorites and associated diagenetic minerals: Authigenesis in modern organic-rich sediments. Marine Geology, 80, 231–267.

German, C.R., and Elderfield, H. (1990) Rare earth elements in the NW Indian Ocean. Geochimica et Cosmochimica Acta, 54, 1929–1940.

German, C.R., Holliday, B.P., and Elderfield, H. (1991) Redox cycling of rare earth elements in the suboxic zone of the Black Sea. Geochimica et Cosmochimica Acta, 55, 3553–3558.

628 Giresse, P., and Odin, G.S. (1973) Nature minéralogique et origine des glauconies du plateau
629 continental du Gabon et du Congo. Sedimentology, 20, 457–488.
630 Gough, D. (1981) Solar interior structure and luminosity variations. Physics of Solar
631 Variations, 74, 21–34
632 Gutjahr, M., Frank, M., Stirling, C.H., Klemm, V., Van de Flierdt, T., and Halliday, A.N.
633 (2007) Reliable extraction of a deepwater trace metal isotope signal from Fe–Mn
634 oxyhydroxide coatings of marine sediments. Chemical Geology, 242, 351–370.
635 Haley, B.A., Klinkhammer, G.P., and McManus, J. (2004) Rare earth elements in pore waters
636 of marine sediments. Geochimica et Cosmochimica Acta, 68, 1265–1279.
637 Hambrey, M.J., and Harland, W.B. (1981) Earth's Pre-Pleistocene Glacial Record. Cambridge
638 University Press, Cambridge, U.K.
639 Harder, H. (1978) Synthesis of iron layer silicate minerals under natural conditions. Clays
640 and Clay Minerals, 26, 65–72.
641 Harder, H., and Flehmig, W. (1970) Quarzsynthese bei tiefen temperaturen. Geochimica et
642 Cosmochimica Acta, 34, 295–300.
643 Hartley, A., Kurjanski, B., Pugsley, J., and Armstrong, J. (2020) Ice-rafting in lakes in the
644 early Neoproterozoic: dropstones in the Diabaig Formation, Torridon Group, NW
645 Scotland. Scottish Journal of Geology, 56, 47–53.
646 Hingston F.J., and Raupach M. (1967) The reaction between monosilicic acid and aluminium
647 hydroxide. I. Kinetics of adsorption of silicic acid by aluminium hydroxide. Australian
648 Journal of Soil Research, 5, 295–309.
649 Hodgskiss, M.S.W., Kunzmann, M., Poirier, A., and Halverson, G.P. (2018) The role of
650 microbial iron reduction in the formation of Proterozoic molar tooth structures. Earth
651 and Planetary Science Letters, 482, 1–11.
652 Hornibrook, E.R., and Longstaffe, F.J. (1996) Berthierine from the lower cretaceous

Clearwater formation, Alberta, Canada. Clays and Clay Minerals, 44, 1–21.

Huang, C.P. (1975) The removal of aqueous silica from dilute aqueous solution. Earth and Planetary Science Letters, 27, 265–274.

Iijima, A., and Matsumoto, R. (1982) Berthierine and chamosite in coal measures of Japan. Clays and Clay Minerals, 30, 264–274.

Isson, T.T., and Planavsky, N.J. (2018) Reverse weathering as a long-term stabilizer of marine pH and planetary climate. Nature, 560, 471–475.

Isson, T.T., Planavsky, N.J., Coogan, L.A., Stewart, E. M., Ague, J.J., Bolton, E.W., Zhang, S., McKenzie, N.R., and Kump, L.R. (2020) Evolution of the global carbon cycle and climate regulation on earth. Global Biogeochemical Cycles, 34, e2018GB006061, DOI: 10.1029/2018GB006061.

Johnson, B.R., Tostevin, R., Gopon, P., Wells, J., Robinson, S.A., and Tosca, N.J. (2020) Phosphorus burial in ferruginous SiO_2-rich Mesoproterozoic sediments. Geology, 48, 92–96.

Kanzaki, Y., and Murakami, T. (2015) Estimates of atmospheric CO_2 in the Neoarchean–Paleoproterozoic from paleosols. Geochimica et Cosmochimica Acta, 159, 190–219.

Kasting, J.F. (1987) Theoretical constraints on oxygen and carbon dioxide concentrations in the Precambrian atmosphere. Precambrian research, 34, 205–229.

——— (2005) Methane and climate during the Precambrian era. Precambrian Research, 137, 119–129.

Kim, J., Dong, H., Seabaugh, J., Newell, S.W., and Eberl, D.D. (2004) Role of microbes in the smectite-to-illite reaction. Science, 303, 830–832.

Kimberley, M.M. (1979) Origin of oolitic iron formations. Journal of Sedimentary Research, 49, 111–132.

——— (1980) The Paz de Rio oolitic inland-sea iron formation. Economic Geology, 75, 97–

106.

Kozłowska, A., and Maliszewska, A. (2015) Berthierine in the Middle Jurassic sideritic rocks from southern Poland. Geological Quarterly, 59, 551–564.

Krissansen-Totton, J., and Catling, D.C. (2020) A coupled carbon-silicon cycle model over Earth history: Reverse weathering as a possible explanation of a warm mid-Proterozoic climate. Earth and Planetary Science Letters, 537, 116181, DOI: 10.1016/j.epsl.2020.116181.

Kuipers, G., Beunk, F.F., and van der Wateren, F.M. (2013) Periglacial evidence for a 1.91–1.89 Ga old glacial period at low latitude. Central Sweden. Geology Today, 29, 218–221.

Lawrence, M.G., Greig, A., Collerson, K.D., and Kamber, B.S. (2006) Rare earth element and yttrium variability in south east Queensland waterways. Aquatic Geochemistry, 12, 39–72.

Lin, Y.T., Tang, D.J., Shi, X.Y., Zhou, X.Q., and Huang, K.J. (2019) Shallow-marine ironstones formed by microaerophilic iron-oxidizing bacteria in terminal Paleoproterozoic. Gondwana Research, 76, 1–18.

Liu, A.Q., Tang, D.J., Shi, X.Y., Zhou, L.M., Zhou, X.Q., Shang, M.H., Li, Y., and Song, H.Y. (2019) Growth mechanisms and environmental implications of carbonate concretions from the ~1.4 Ga Xiamaling Formation, North China. Journal of Palaeogeography, 8, DOI: 10.1186/s42501-019-0036-4.

Logvinenko, N.V. (1982) Origin of glauconite in the recent bottom sediments of the ocean. Sedimentary Geology, 31, 43–48.

Luo, G.M., Hallmann, C., Xie, S.C., Ruan, X.Y., and Summons, R.E. (2015) Comparative microbial diversity and redox environments of black shale and stromatolite facies in the Mesoproterozoic Xiamaling Formation. Geochimica et Cosmochimica Acta 151, 150–167.

703 Mackenzie, F.T., and Garrels, R.M. (1966) Chemical mass balance between rivers and oceans.
704 American Journal of Science, 264, 507–525.
705 Mackenzie, F.T., and Kump, L.R. (1995) Reverse weathering, clay mineral formation, and
706 oceanic element cycles. Science, 270, 586.
707 Maliva, R.G., Knoll, A.H., and Simonson, B.M. (2005) Secular change in the Precambrian
708 silica cycle: Insights from chert petrology. Geological Society of America Bulletin, 117,
709 835–845.
710 Maynard, J.B. (1986) Geochemistry of oolitic iron ores, an electron microprobe study.
711 Economic Geology, 81, 1473–1483.
712 McRae, S.G. (1972) Glauconite. Earth-Science Reviews, 8, 397–440.
713 Meng, Q.R., Wei, H.H., Qu, Y.Q., and Ma, S.X. (2011) Stratigraphic and sedimentary records
714 of the rift to drift evolution of the northern North China craton at the Paleo- to
715 Mesoproterozoic transition. Gondwana Research, 20, 205–218.
716 Meunier, A., and El Albani, A. (2007) The glauconite-Fe-illite-Fe-smectite problem: a critical
717 review. Terra Nova, 19, 95–104.
718 Michalopoulos, P., and Aller, R.C. (1995) Rapid clay mineral formation in Amazon delta
719 sediments: reverse weathering and oceanic elemental cycles. Science, 270, 614–617.
720 Muhling, J.R., and Rasmussen, B. (2020) Widespread deposition of greenalite to form
721 Banded Iron Formations before the Great Oxidation Event. Precambrian Research, 339,
722 DOI: 10.1016/j.precamres.2020.105619.
723 Mücke, A. (2006) Chamosite, siderite and the environmental conditions of their formation in
724 chamosite-type Phanerozoic ooidal ironstones. Ore Geology Reviews, 28, 235–249.
725 Odin, G.S. (1988) Green Marine Clays: Oolitic Ironstone Facies, Verdine Facies, Glaucony
726 Facies and Celadonite-Bearing Rock Facies–A Comparative Study, 455 p. Elsevier,
727 Amsterdam.

Odin, G.S., and Létolle, R. (1980) Glauconitization and Phosphatization Environments a Tentative Comparison. The Society of Economic Paleontologists and Mineralogists, 29, 227–237.

Odin, G.S., and Matter, A. (1981) Origin of Glauconite (De glauconiarum origine). Sedimentology, 28, 611–641.

Olson, S.L., Reinhard, C.T., and Lyons, T.W. (2016) Limited role for methane in the mid-Proterozoic greenhouse. Proceedings of the National Academy of Sciences, 113, 11447–11452.

Pavlov, A.A., Hurtgen, M.T., Kasting, J.F., and Arthur, M.A. (2003) Methane-rich Proterozoic atmosphere? Geology, 31, 87–90.

Planavsky, N., Bekker, A., Rouxel, O.J., Kamber, B., Hofmann, A., Knudsen, A., and Lyons, T.W. (2010) Rare earth element and yttrium compositions of Archean and Paleoproterozoic Fe formations revisited: New perspectives on the significance and mechanisms of deposition. Geochimica et Cosmochimica Acta, 74, 6387–6405.

Planavsky, N.J., McGoldrick, P., Scott, C.T., Li, C., Reinhard, C.T., Kelly, A.E., Chu, X.L., Bekker, A., Love, G.D., and Lyons, T.W. (2011) Widespread iron-rich conditions in the mid-Proterozoic ocean. Nature, 477, 448–451.

Porrenga, D.H. (1967) Glauconite and chamosite as depth indicators in the marine environment. Marine Geology, 5, 495–501.

Poulton, S.W., and Canfield, D.E. (2011) Ferruginous conditions: a dominant feature of the ocean through Earth's history. Elements, 7, 107–112.

Pu, J.P., Bowring, S.A., Ramezani, J., Myrow, P., Raub, T.D., Landing, E., Mills, A., Hodgin, E., and Macdonald, F.A. (2016) Dodging snowballs: Geochronology of the Gaskiers glaciation and the first appearance of the Ediacaran biota. Geology, 44, 955–958.Rasmussen, B., Muhling, J.R., Suvorova, A., and Krapež, B. (2017) Greenalite

753 precipitation linked to the deposition of banded iron formations downslope from a late
754 Archean carbonate platform. Precambrian Research, 290, 49–62.
755 Rivas-Sanchez, M.L., Alva-Valdivia, L.M., Arenas-Alatorre, J., Urrutia-Fucugauchi, J., Ruiz-
756 Sandoval, M., and Ramos-Molina, M.A. (2006) Berthierine and chamosite hydrothermal:
757 genetic guides in the Peña Colorada magnetite-bearing ore deposit, Mexico. Earth
758 Planets Space, 58, 1389–1400.
759 Roberson, A.L., Roadt, J., Halevy, I., and Kasting, J.F. (2011) Greenhouse warming by
760 nitrous oxide and methane in the Proterozoic Eon. Geobiology, 9, 313–320.
761 Rohrlich, V., Price, N.B., and Calvert, S.E. (1969) Chamosite in the recent sediments of Loch
762 Etive, Scotland. Journal of Sedimentary Research, 39, 624–631.
763 Rooney, A.D., Strauss, J.V., Brandon, A.D., and Macdonald, F.A. (2015) A Cryogenian
764 chronology: Two long-lasting synchronous Neoproterozoic glaciations. Geology, 43,
765 459–462.
766 Ryan, P.C., and Reynolds Jr., R.C. (1996) The origin and diagenesis of grain-coating
767 serpentine-chlorite in Tuscaloosa Formation sandstone, US Gulf Coast. American
768 Mineralogist, 81, 213–225.
769 Sheldon, N.D. (2006) Precambrian paleosols and atmospheric CO_2 levels. Precambrian
770 Research, 147, 148–155.
771 Sigg, L., and Stumm, W. (1981) The interaction of anions and weak acids with the hydrous
772 goethite (α-FeOOH) surface. Colloids and surfaces, 2, 101–117.
773 Sperling, E.A., Wolock, C.J., Morgan, A.S., Gill, B.C., Kunzmann, M., Halverson, G.P.,
774 Macdonald, F.A., Knoll, A.H., and Johnston, D.T. (2015) Statistical analysis of iron
775 geochemical data suggests limited late Proterozoic oxygenation. Nature, 523, 451–454.
776 Stanton, C.L., Reinhard, C.T., Kasting, J.F., Ostrom, N.E., Haslun, J.A., Lyons, T.W., and
777 Glass, J.B. (2018) Nitrous oxide from chemodenitrification: A possible missing link in

778 the Proterozoic greenhouse and the evolution of aerobic respiration. Geobiology, 16,
779 597–609.
780 Tang, D.J., Shi, X.Y., Wang, X.Q., and Jiang, G.Q. (2016) Extremely low oxygen
781 concentration in mid-Proterozoic shallow seawaters. Precambrian Research, 276, 145–
782 157.
783 Tang, D.J., Shi, X.Y., Ma, J.B., Jiang, G.Q., Zhou, X.Q., and Shi, Q. (2017a) Formation of
784 shallow-water glaucony in weakly oxygenated Precambrian ocean: An example from the
785 Mesoproterozoic Tieling Formation in North China. Precambrian Research, 294, 214–
786 229.
787 Tang, D.J., Shi, X.Y., Jiang, G.Q., Zhou, X.Q., and Shi, Q. (2017b) Ferruginous seawater
788 facilitates the transformation of glauconite to chamosite: An example from the
789 Mesoproterozoic Xiamaling Formation of North China. American Mineralogist, 102,
790 2317–2332.
791 Tang, D.J., Shi, X.Q., Jiang, G.Q., Wu, T., Ma, J.B., and Zhou, X.Q. (2018) Stratiform
792 siderites from the Mesoproterozoic Xiamaling Formation in North China. Genesis and
793 environmental implications. Gondwana Research, 58, 1–15.
794 Tang, D.J., Ma, J.B., Shi, X.Y., Lechte, M., and Zhou, X.Q. (2020) The formation of marine
795 red beds and iron cycling on the Mesoproterozoic North China Platform. American
796 Mineralogist, 105, 1412–1423.
797 Tosca, N.J., Guggenheim, S., and Pufahl, P.K. (2016) An authigenic origin for Precambrian
798 greenalite: Implications for iron formation and the chemistry of ancient seawater.
799 Geological Society of America Bulletin, 128, 511–530.
800 Taylor, K.G. (1990). Berthierine from the non-marine Wealden (Early Cretaceous) sediments
801 of south-east England. Clay Minerals, 25, 391–399.
802 Taylor, K.G., and Curtis, C.D. (1995) Stability and facies association of early diagenetic

mineral assemblages; an example from a Jurassic ironstone-mudstone succession, U.K. Journal of Sedimentary Research, 65, 358–368.

Van Houten, F.B., and Purucker, M.E. (1984) Glauconitic peloids and chamositic ooids-favorable factors, constraints, and problems. Earth-Science Reviews, 20, 211–243.

——— (1985) On the origin of glauconitic and chamositic granules. Geo-marine letters, 5, 47–49.

Velde, B. (1995) Origin and Mineralogy of Clays: Clays and Environment, 334 p. Springer-Verlag, Berlin, Heidelberg.

Visser, J.N.J. (1971) The deposition of the Griqualand glacial member in the Transvaal Supergroup. Transactions of the Geological Society of South Africa, 74, 187–199.

Walker, J.C.G., Hays, P.B., and Kasting, J.F. (1981) A negative feedback mechanism for the long-term stabilization of Earth's surface temperature. Journal of Geophysical Research: Oceans, 86, 9776–9782.

Warke, M.R., Di Rocco, T., Zerkle, A.L., Lepland, A., Prave, A.R., Martin, A.P., Ueno, Y., Condon, D.J., and Claire, M.W. (2020) The Great Oxidation Event preceded a Paleoproterozoic "snowball Earth". Proceedings of the National Academy of Sciences, 117, 13314–13320.

Wang, H.Z., Chu, X.C., Liu, B.P., Hou, H.F., and Ma, L.F. (1985) Atlas of the Palaeogeography of China, 143p. Cartographic Publishing House, Beijing (in Chinese and English).

Wang, X.M., Zhang, S.C., Wang, H.J., Su, J., He, K., Wang, Y., and Wang, X.Q. (2017) Significance of source rock heterogeneities: A case study of Mesoproterozoic Xiamaling Formation shale in North China. Petroleum Exploration and Development, 44, 32–39.

Williams, G.E. (2005) Subglacial meltwater channels and glaciofluvial deposits in the Kimberley Basin, Western Australia: 1.8 Ga low-latitude glaciation coeval with

continental assembly. Journal of the Geological Society, 162, 111–124.

Young, T.P. (1989) Phanerozoic ironstones: An introduction and review. Geological Society Special Publication, 46, ix–xxv.

Zhang, S.C., Wang, X.M., Hammarlund, E.U., Wang, H.J., Costa, M.M., Bjerrum, C.J., Connelly, J.N., Zhang, B.M., Bian, L.Z., and Canfield, D.E. (2015) Orbital forcing of climate 1.4 billion years ago. Proceedings of the National Academy of Sciences, 112, E1406–E1413.

Zhang, S.C., Wang, X.M., Wang, H.J., Bjerrum, C.J., Hammarlund, E.U., Costa, M.M., Connelly, J.N., Zhang, B.M., Su, J., and Canfield, D.E. (2016) Sufficient oxygen for animal respiration 1,400 million years ago. Proceedings of the National Academy of Sciences, 113, 1731–1736.

Zhang, S.H., Zhao, Y., Yang, Z.Y., He, Z.F., and Wu, H. (2009) The 1.35 Ga diabase sills from the Northern North China Craton: Implications for breakup of the Columbia (Nuna) supercontinent. Earth and Planetary Science Letters, 288, 588–600.

Zhang, S.H., Zhao, Y., and Santosh, M. (2012a) Mid-Mesoproterozoic bimodal magmatic rocks in the northern North China Craton: Implications for magmatism related to breakup of the Columbia supercontinent. Precambrian Research, 222, 339–367.

Zhang, S.H., Li, Z.X., Evans, D.A.D., Wu, H.C., Li, H.Y., and Dong, J. (2012b) Pre-Rodinia supercontinent Nuna shaping up: A global synthesis with new paleomagnetic results from North China. Earth and Planetary Science Letters, 353, 145–155.

Zhang, S.H., Zhao, Y., Li, X.H., Ernst, R.E., and Yang, Z.Y. (2017) The 1.33–1.30 Ga Yanliao large igneous province in the North China Craton: Implications for reconstruction of the Nuna (Columbia) supercontinent, and specifically with the North Australian Craton. Earth and Planetary Science Letters, 465, 112–125.

Zhao, G.C., Sun, M., Wilde, S.A., and Li, S.Z. (2003) Assembly, accretion and breakup of the

Paleo-Mesoproterozoic Columbia supercontinent: Records in the North China Craton. Gondwana Research, 6, 417–434.

——— (2004) A Paleo-Mesoproterozoic supercontinent: Assembly, growth and breakup. Earth-Science Reviews, 67, 91–123.

Zhao, G.C., Li, S.Z., Sun, M., and Wilde, S.A. (2011) Assembly, accretion, and break- up of the Palaeo-Mesoproterozoic Columbia supercontinent: records in the North China Craton revisited. International Geology Review, 53, 1331–1356.

Zhou, C.M., Huyskens, M.H., Lang, X.G., Xiao, S.H., and Yin, Q.Z. (2019) Calibrating the terminations of Cryogenian global glaciations. Geology, 47, 251–254.

Zhou, L.M., Wang, R., Hou, Z.Q., Li, C., Zhao, H., Li, X.W., and Qu, W.J. (2018) Hot Paleocene-Eocene Gangdese arc, Growth of continental crust in southern Tibet. Gondwana Research, 62, 178–197.

FIGURE AND TABLE CAPTIONS

Figure 1. Geological setting. (**a**) Major tectonic subdivisions of China showing the location of the study area. (**b**) Simplified paleogeographic map of North China during Mesoproterozoic, showing the location of the studied area (modified after Wang et al. 1985). (**c**) Simplified geological map of the studied section (modified after the 1:200,000 Geological Map of China, The China Geological Survey, 2013).

Figure 2. Stratigraphic columns of the Xiamaling Formation at Zhaojiashan village, Huailai County and Tielingzi village, Jixian county, North China, showing the studied glauconite-berthierine-rich interval. The boundary between the siliciclastic-dominated Xiamaling Formation and the carbonate-dominated Tieling Formation is shown. In the Jixian section, the upper part of Member I of the Xiamaling formation is not preserved, so the correlation

878 between Jixian and Huailai section is estimated. The geochronological constrains were
879 adopted from Zhang et al. (2015).
880
881 **Figure 3.** Field photographs showing major depositional facies in Member I of the Xiamaling
882 Formation at Jixian. (**a**) Black and green silty shales of the lower Xiamaling Formation. (**b**)
883 Disconformity between Tieling and Xiamaling formations. The upper Tieling Formation is
884 characterized by argillaceous limestone, while the basal Xiamaling Formation is composed of
885 iron-rich silty mudstone and siltstone. (**c**) Close view of alternating iron-rich silt mudstone
886 and siltstone (arrows) in the basal of the Xiamaling Formation. (**d**) Close view of the iron-
887 rich silty mudstone. (**e**) Close view of the dark green, iron-rich (glauconite-rich) siltstones. (**f**)
888 A polished slab showing the green sands and pebbles detached from muddy (glauconite-rich)
889 siltstone. (**g**) Field photographs showing black to gray silty shales. (**h**) Close view of muddy
890 (berthierine-rich) siltstone. (**i**) A polished slab of berthierine-rich siltstone showing gray and
891 white lamination. (**j**) Gray silty shale interbedded with siderite-concretion-rich layers (the
892 lower arrow) and siderite packstone bands (the upper arrow). (**k**) Siderite concretion
893 surrounded by silty shale laminae. (**l**) A sandstone band with cross-bedding (arrows). (**m**)
894 Green silty shale with abundant quartz sandstone bands (arrows).
895
896 **Figure 4.** Microscopic features of layered berthierine and glauconite from the Xiamaling
897 Formation, North China. (**a**) A photomicrograph showing that upper glauconite sands and
898 pebbles were detached from lower muddy siltstone layers (Gl = glauconite, Q = quartz). (**b**)
899 Pebble-bearing sandstone layer, showing glauconite sands and pebbles detached from muddy
900 siltstone (Gl = glauconite, Q = quartz). (**c**) Alternation of berthierine rich siltstone layer (SL)
901 and detrital clay mineral rich silty mudstone layer (ML). (**d**) Close view of lamination in
902 panel **c**, SL = berthierine rich siltstone layer, ML = detrital clay mineral rich silty mudstone

903 layer. (**e**) Cross bedding in berthierine rich siltstone. (**f**) Siderite grains trapped by siltstone
904 laminae (arrows). (**g**) Siderite grains in a siderite concretion (e.g., Figure 3k). (**h**) Siderite
905 sands in a packstone band (e.g., Figure 3j).
906
907 **Figure 5.** Results of XRD and TEM analyses of gray and green siltstone from the Xiamaling
908 Formation, North China. (**a**) XRD analysis results showing that gray siltstone is rich in
909 berthierine but poor in glauconite, while green siltstone is the reverse. (**b**) TEM images of
910 berthierine stratification showing lattice fringe with ~0.73 nm periodicity. (**c**) TEM images of
911 berthierine-chamosite stratification showing lattice fringes with ~14.4 and ~0.73 nm
912 periodicities, respectively. (**d**) TEM images of glauconite stratification showing lattice fringes
913 with ~1.03 nm periodicity. (**e**) TEM images of berthierine-glauconite interstratification
914 showing lattice fringes with ~0.70 and ~1.0 nm periodicities, respectively.
915
916 **Figure 6.** Results of SEM and EBSD analyses of green and gray siltstone from the Xiamaling
917 Formation, North China. (**a**) Glauconite-rich layer, showing detrital grains within glauconite
918 matrix. (**b**) Higher magnification BSE image of panel **a**. (**c**) Higher magnification BSE image
919 of glauconite-rich matrix surrounding detrital grains. (**d**) Sand-bearing berthierine-rich layers
920 (light) alternation with berthierine-poor muddy layers (dark). (**e**) Sand-bearing berthierine-
921 rich layers (light) alternation with berthierine-poor muddy layers (dark), showing berthierine-
922 rich layers rich in detrital sands. (**f**) Radiating fans of "bowtie" berthierine in a berthierine-
923 rich layer. (**g**) Berthierine sands detached from berthierine-rich layers. (**h**) Berthierine sand
924 with curved shape (arrows). (**i**) Flame structures caused by berthierine-poor mudstone layer
925 penetrating into berthierine-rich siltstone layer (arrows). (**j**) Detrital grains within berthierine
926 matrix. (**k**) A vertically oriented (unstable) quartz grain (arrow) preserved in a berthierine
927 matrix. (**l**) BSE image showing that detrital quartz, feldspar, and mica in berthierine matrix

928 are not obviously re-dissolved. (**m**) A subhedral hematite nanoparticle in a siderite concretion.
929 (**n**) Aggregated globular hematites in a siderite concretion. (**o**) EBSD analysis of
930 nanoparticles, confirming their hematite composition. F = feldspar, G = glauconite, B =
931 berthierine, M = mica, Q = quartz.
932
933 **Figure 7.** Element mapping analysis results, showing detrital quartz and feldspar grains
934 hosted in the berthierine matrix.
935
936 **Figure 8.** Geochemical analysis results of berthierine-rich and glauconite-rich layers from the
937 Xiamaling Formation, North China. (**a**) Cross plot of K_2O vs. TFe_2O_3; (**b**) Cross plot of SiO_2
938 vs. TFe_2O_3; (**c**) Cross plot of MgO vs. TFe_2O_3; (**d**) Cross plot of Al_2O_3 vs. TFe_2O_3. (**e**)
939 REE+Y patterns of glauconite-rich layer, showing the positive Ce anomalies and low Y/Ho
940 ratios. (**f**) REE+Y patterns of berthierine-rich layer, showing the positive Ce anomalies and
941 low Y/Ho ratios.
942
943 **Figure 9.** A proposed depositional model for the Xiamaling berthierine-rich and glauconite-
944 rich layers. Fe(II) is transported from deep seawater to shallow seawater above storm wave
945 base, and subsequently oxidized by O_2 around the redoxcline, resulting in the precipitation of
946 $Fe(OH)_3$. The accumulation of $Fe(OH)_3$ on the seafloor, and the subsequent increase in pH
947 caused by the dissimilatory reduction (DIR) of this iron, could result in the enrichment of
948 $SiO_{2(aq)}$, $Al(OH)_3$, and $Fe(OH)_2$ near the sediment–seawater interface and the formation of a
949 $Fe(OH)_3$-SiO_2-$Al(OH)_3$-$Fe(OH)_2$ gel. The ageing of this gel results in the formation of
950 berthierine and glauconite. The transformation of glauconite-rich layers to berthierine-rich
951 laminae is likely caused by an increased Fe(II) supply (due to upwelling), which increases the
952 Fe/Si and Fe(II)/TFe ratios.

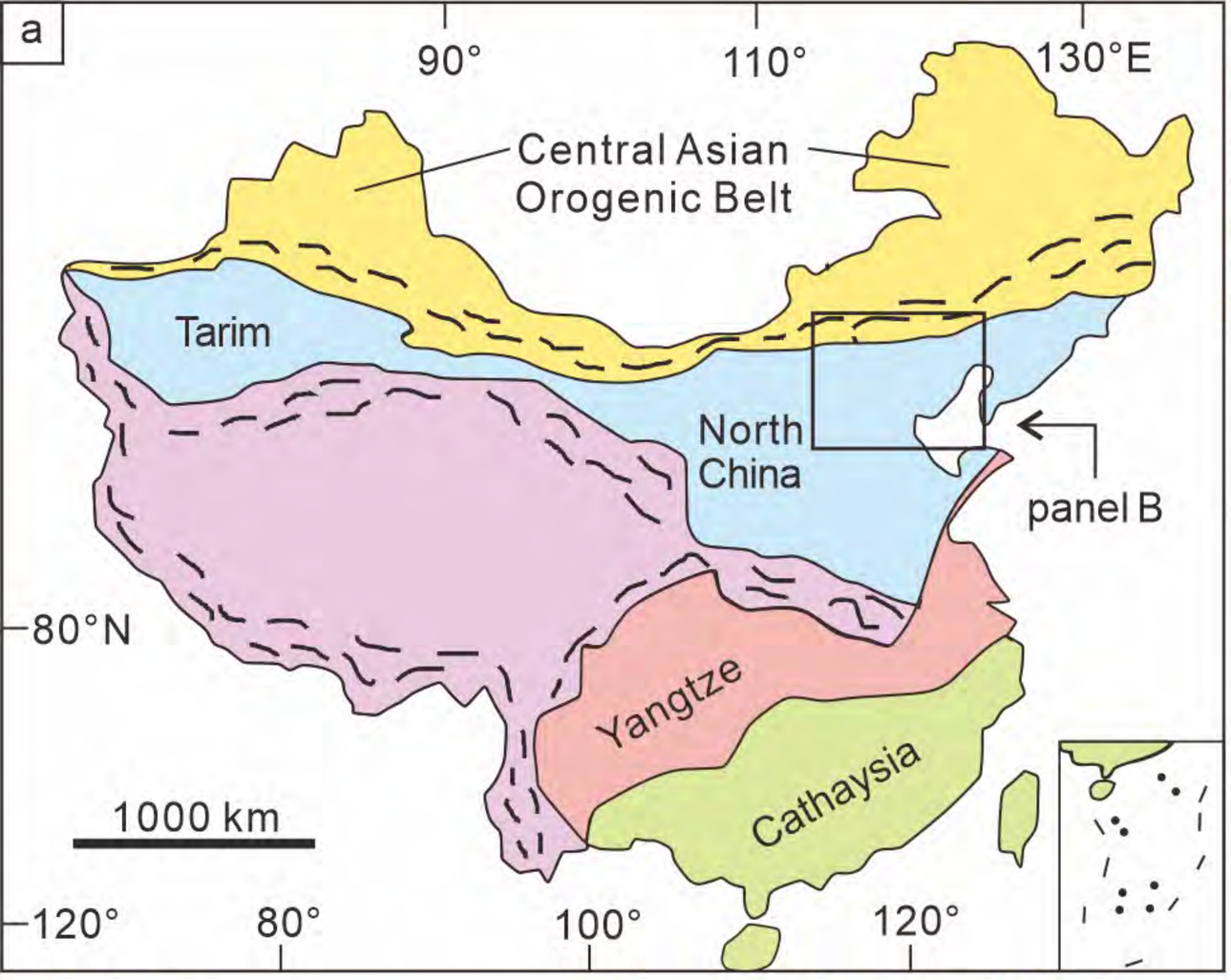
a
90°
110°
130°E
Central Asian
Orogenic Belt
Tarim
North
China
panel B
80°N
Yangtze
Cathaysia
1000 km
120°
80°
100°
120°

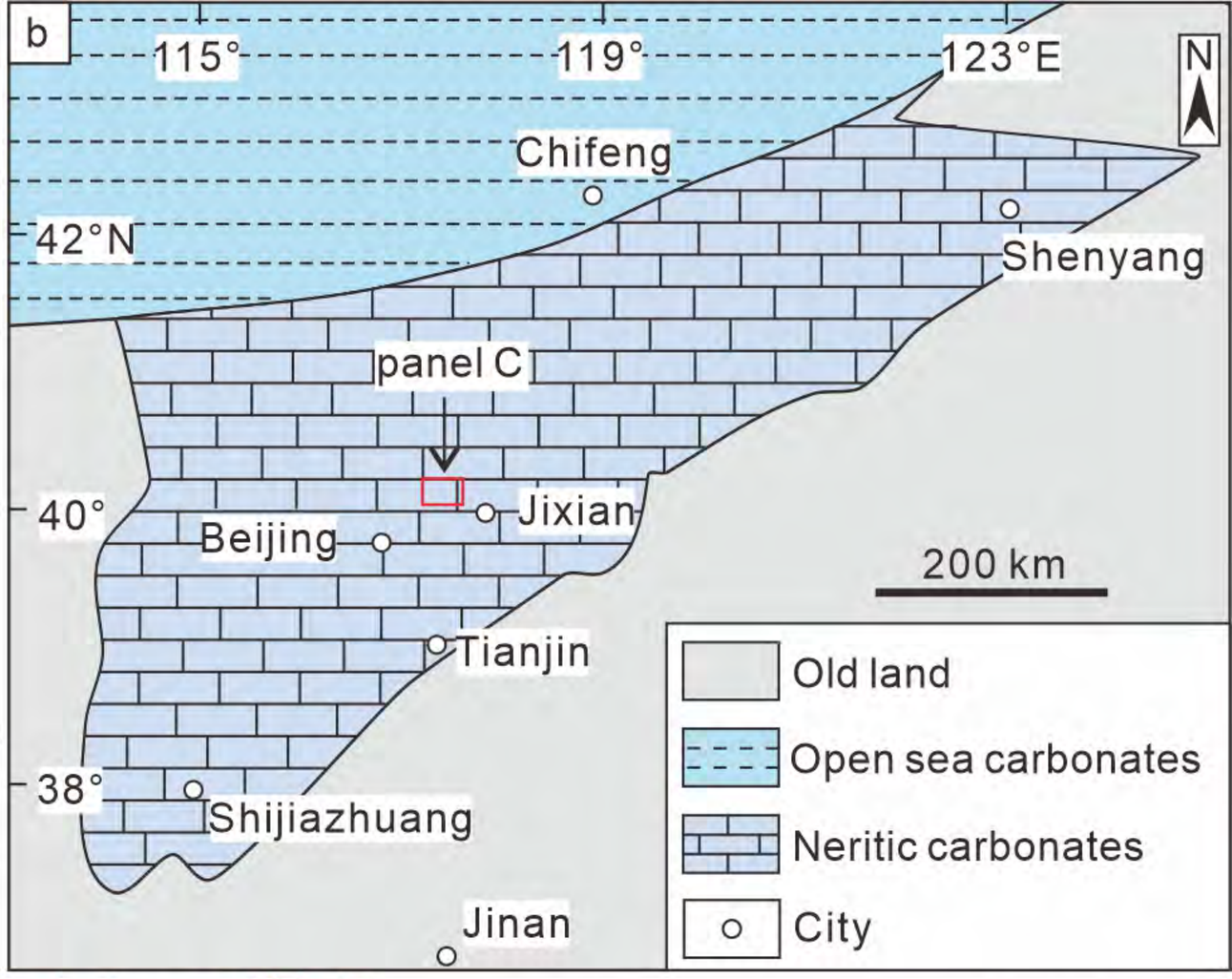
b
115°
119°
123°E
N
Chifeng
Shenyang
42°N
panel C
40°
Beijing
Jixian
200 km
Tianjin
38°
Shijiazhuang
Jinan
Old land
Open sea carbonates
Neritic carbonates
City

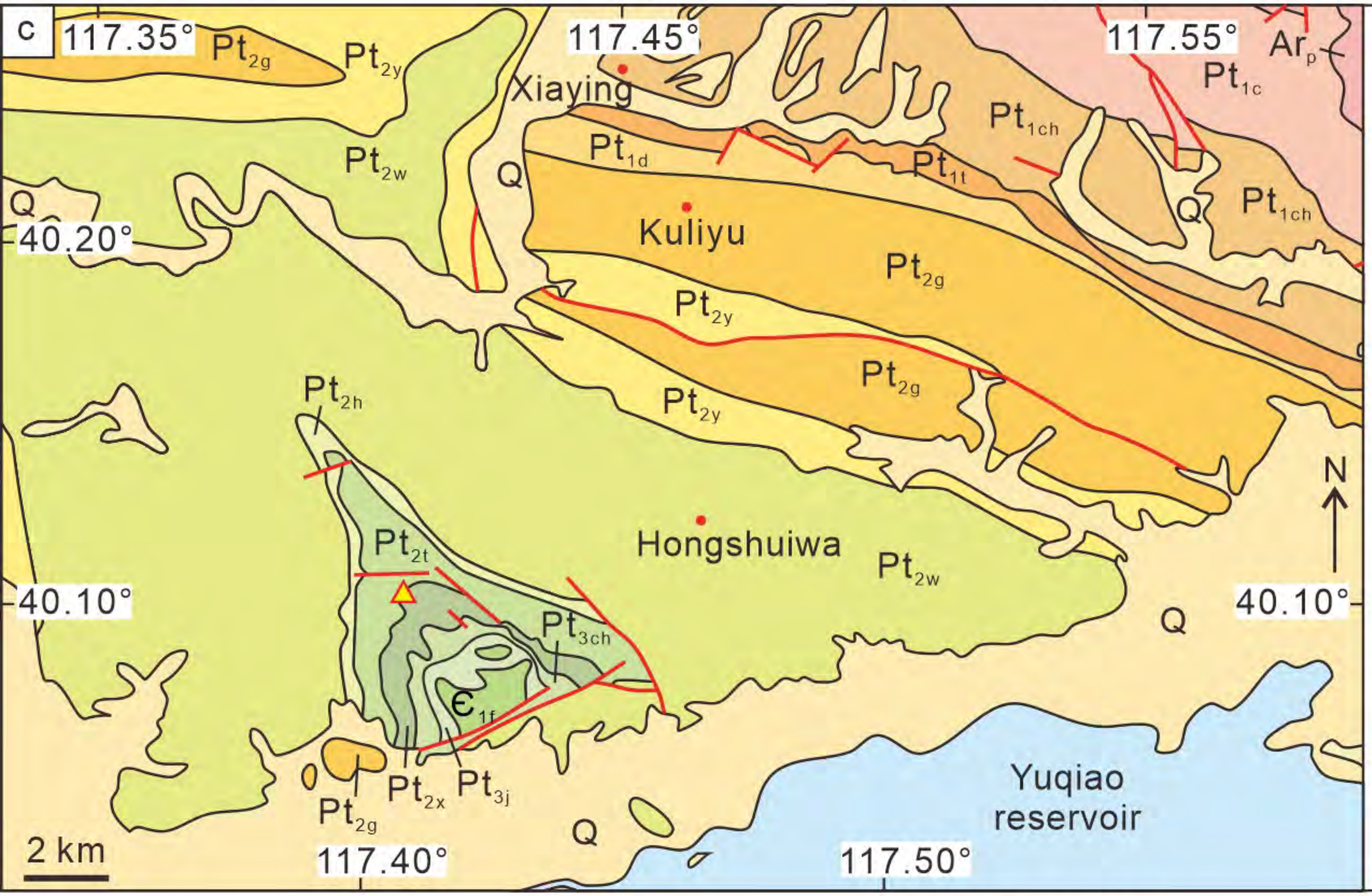
c
117.35°
117.45°
117.55°
Xiaying
Kuliyu
Hongshuiwa
40.20°
40.10°
N
2 km
117.40°
117.50°
Yuqiao
reservoir


Paomachang Formation
Changzhougou Formation
Chuanlinggou Formation
Tuanshanzi Formation
Dahongyu Formation
Gaoyuzhuang Formation
Yangzhuang Formation
Hongshuizhuang Formation
Wumishan Formation
Tieling Formation
Xiamaling Formation
Chang-longshan Formation
Jing'eryu Formation
Fujunshan Formation
Quaternary deposition
Yuqiao reservoir
Fault
Village
Sampling location

Figure 1

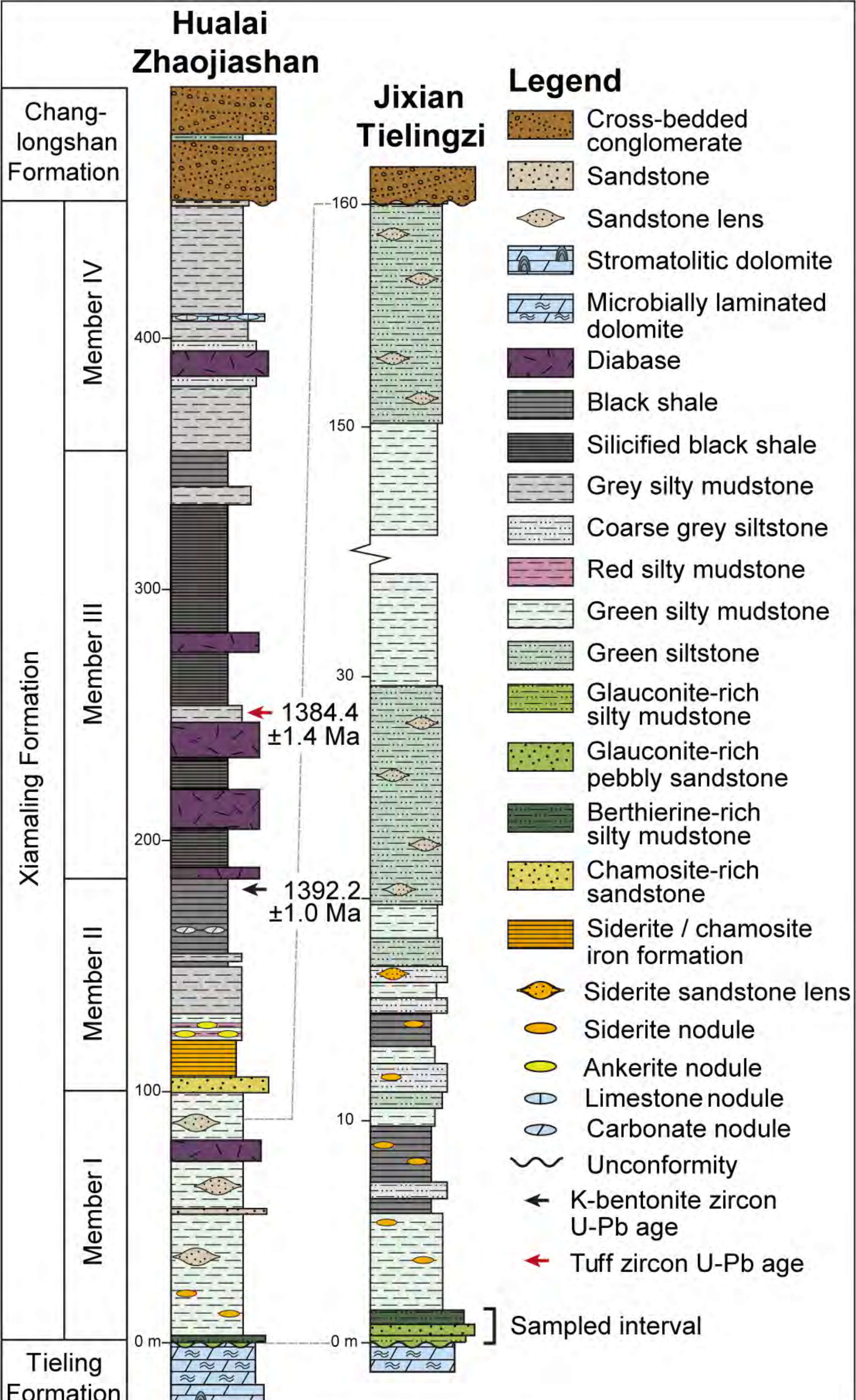
Hualai
Zhaojiashan
Jixian
Tielingzi
Changlongshan Formation
Xiamaling Formation
Member IV
Member III
Member II
Member I
Tieling Formation
400
300
200
100
0 m
160
150
30
10
0 m
1384.4
±1.4 Ma
1392.2
±1.0 Ma
Legend
Cross-bedded conglomerate
Sandstone
Sandstone lens
Stromatolitic dolomite
Microbially laminated dolomite
Diabase
Black shale
Silicified black shale
Grey silty mudstone
Coarse grey siltstone
Red silty mudstone
Green silty mudstone
Green siltstone
Glauconite-rich silty mudstone
Glauconite-rich pebbly sandstone
Berthierine-rich silty mudstone
Chamosite-rich sandstone
Siderite / chamosite iron formation
Siderite sandstone lens
Siderite nodule
Ankerite nodule
Limestone nodule
Carbonate nodule
Unconformity
K-bentonite zircon U-Pb age
Tuff zircon U-Pb age
Sampled interval

Figure 2


a
2 m

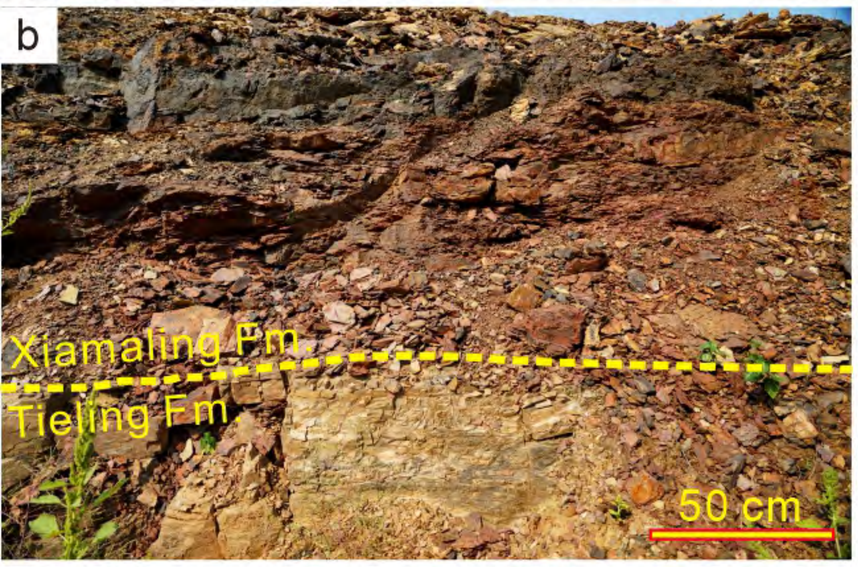
b
Xiamaling Fm
Tieling Fm
50 cm


c
25 cm


d
10 cm


e
50 cm


f
1 cm


g
2 m

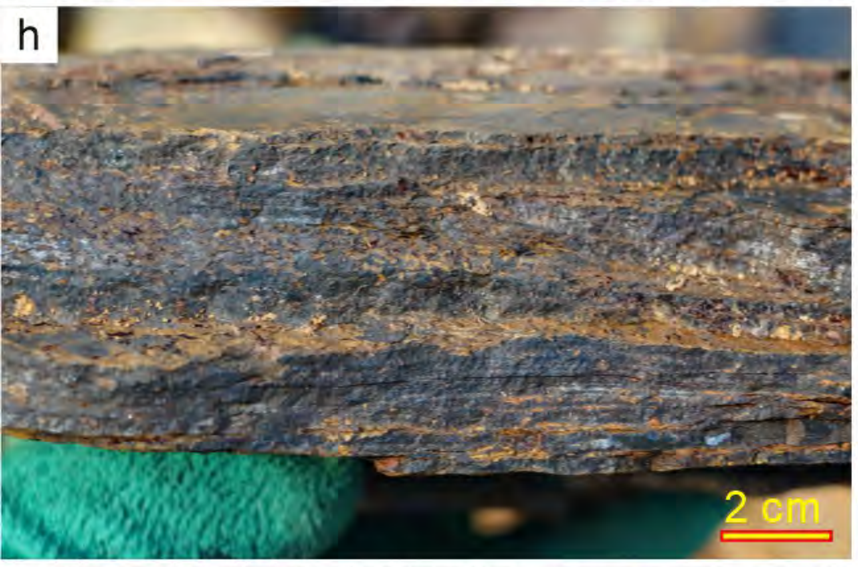
h
2 cm


i
2 cm

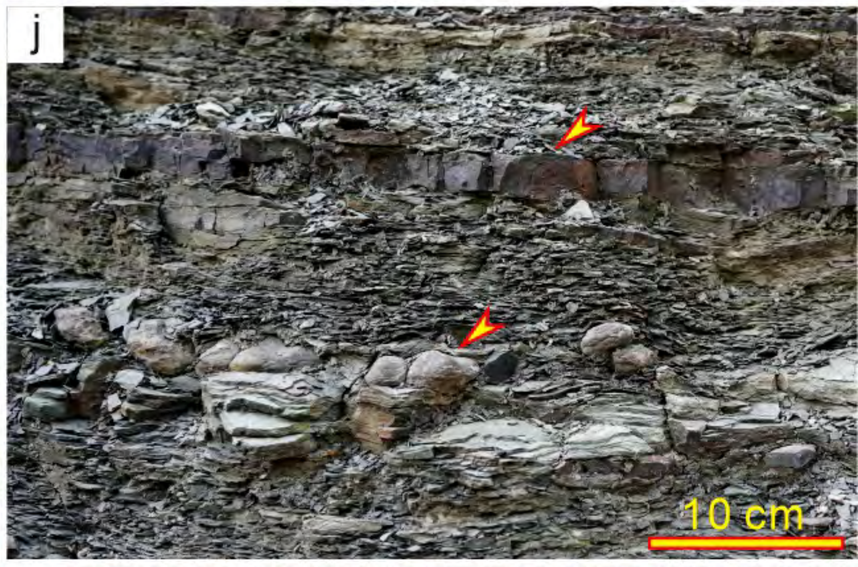
j
10 cm


k
4 cm


l
2 cm


m
10 cm

Figure 3

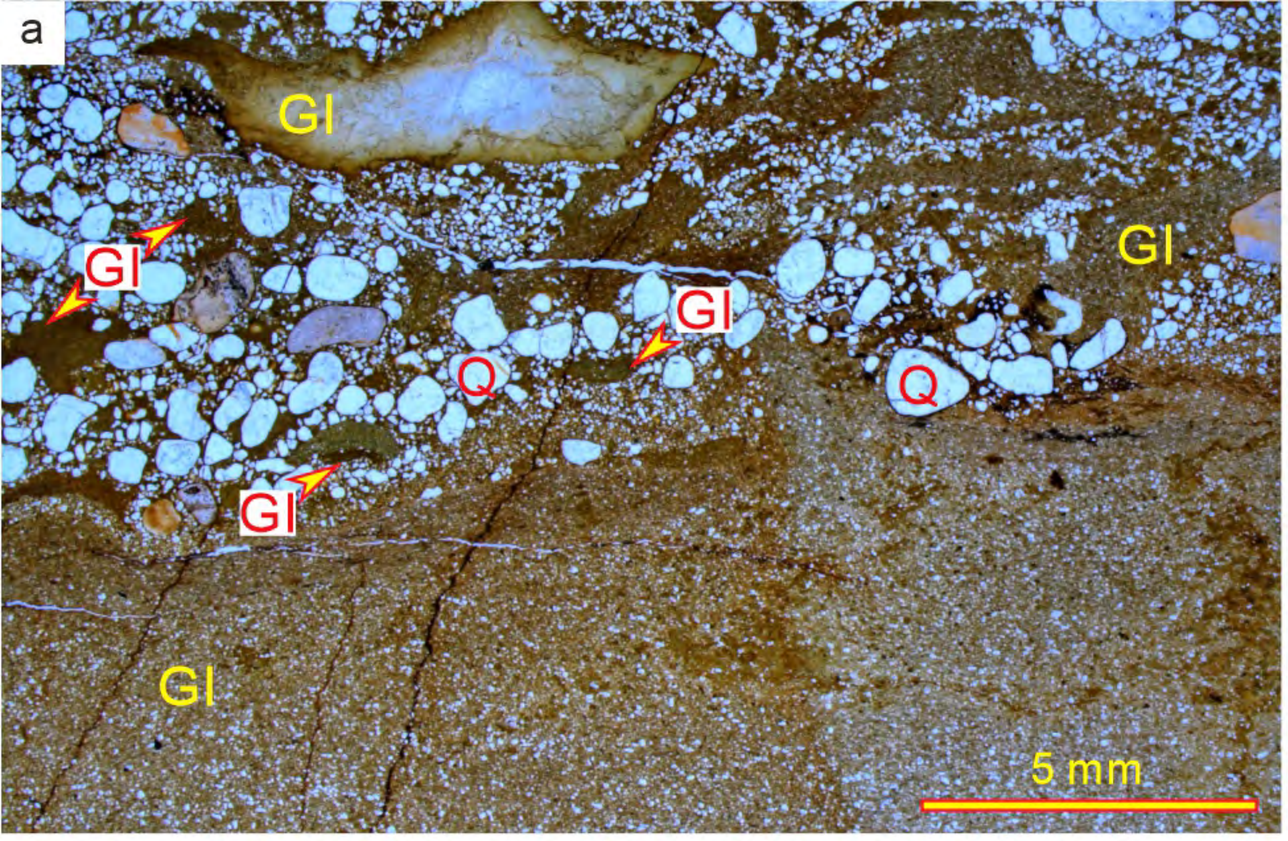
a
Gl
Gl
Gl
Q
Gl
Q
Gl
5 mm

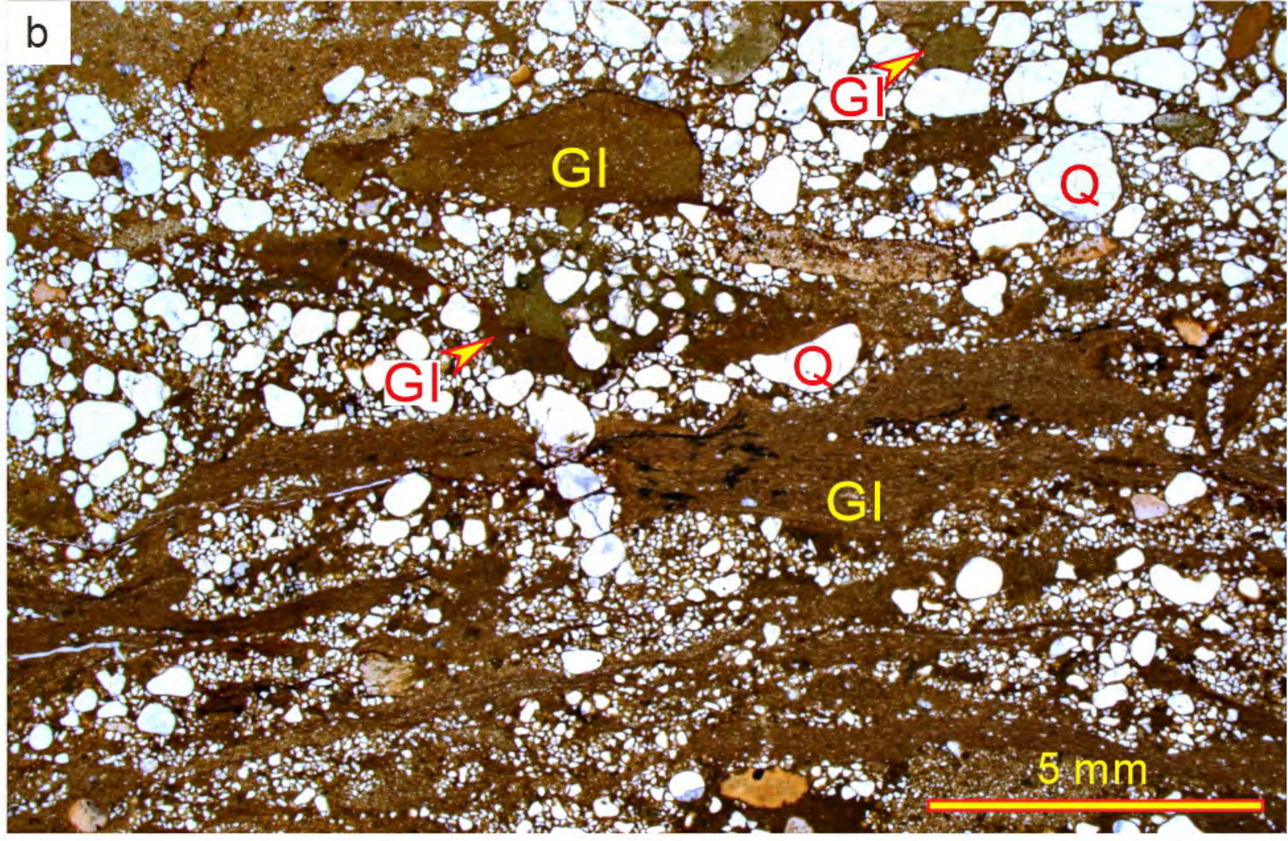
b
Gl
Gl
Q
Gl
Q
Gl
5 mm

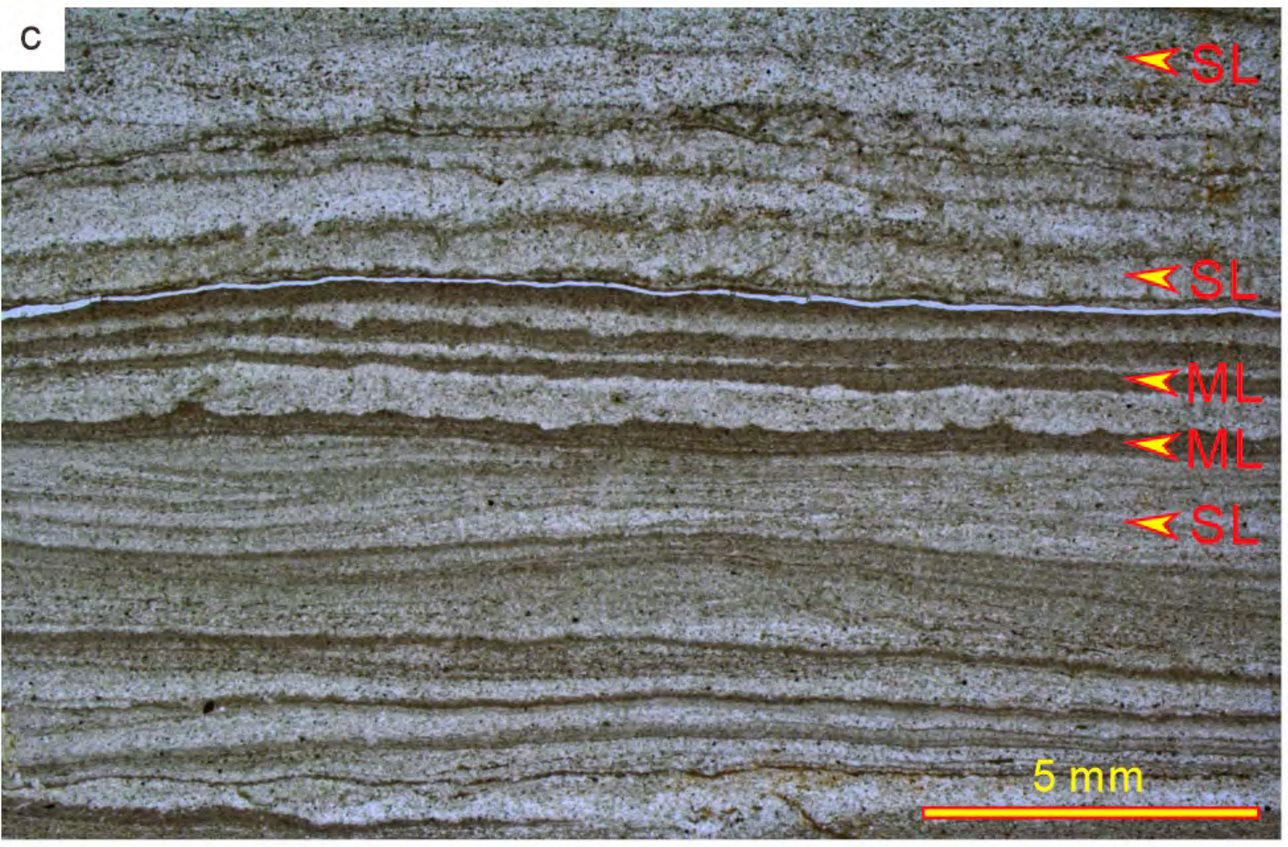
c
SL
SL
ML
ML
SL
5 mm

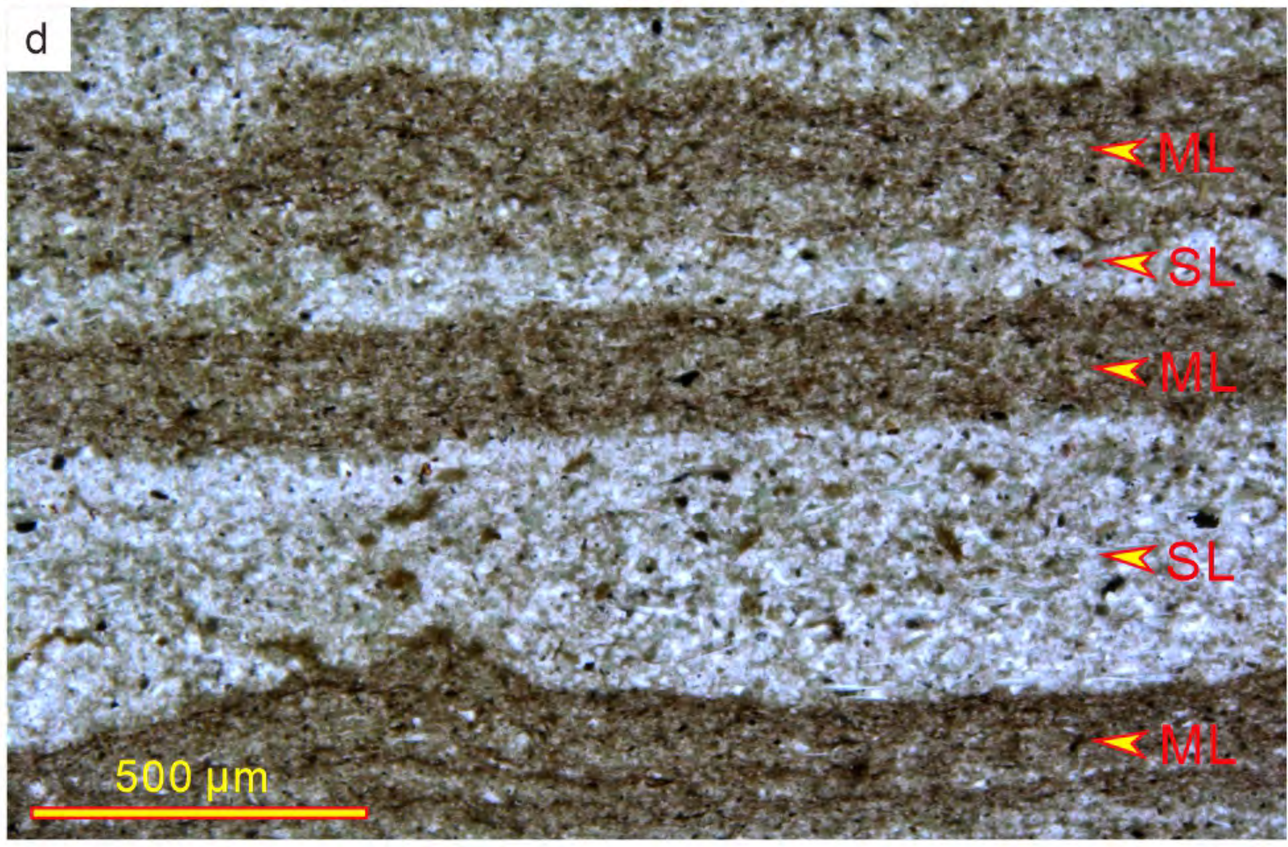
d
ML
SL
ML
SL
ML
500 µm

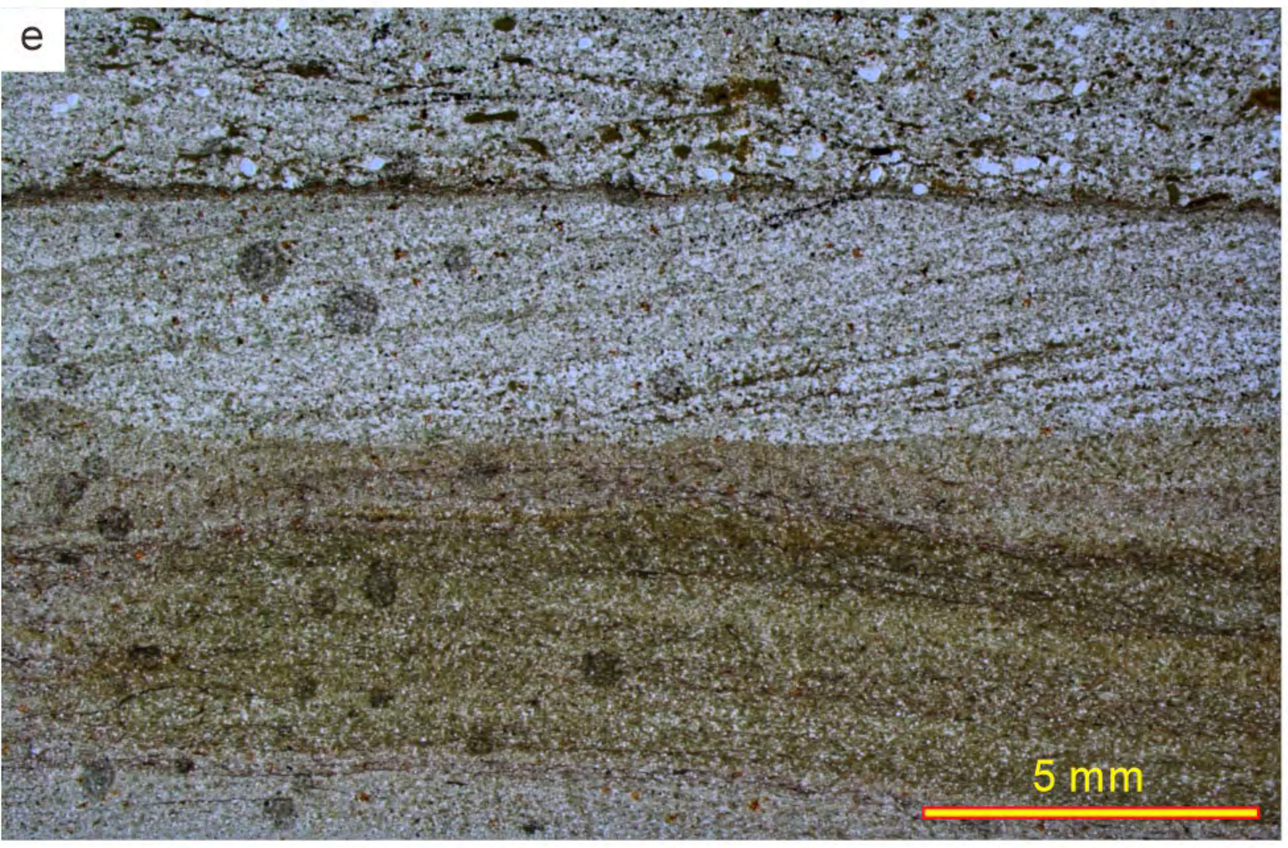
e
5 mm

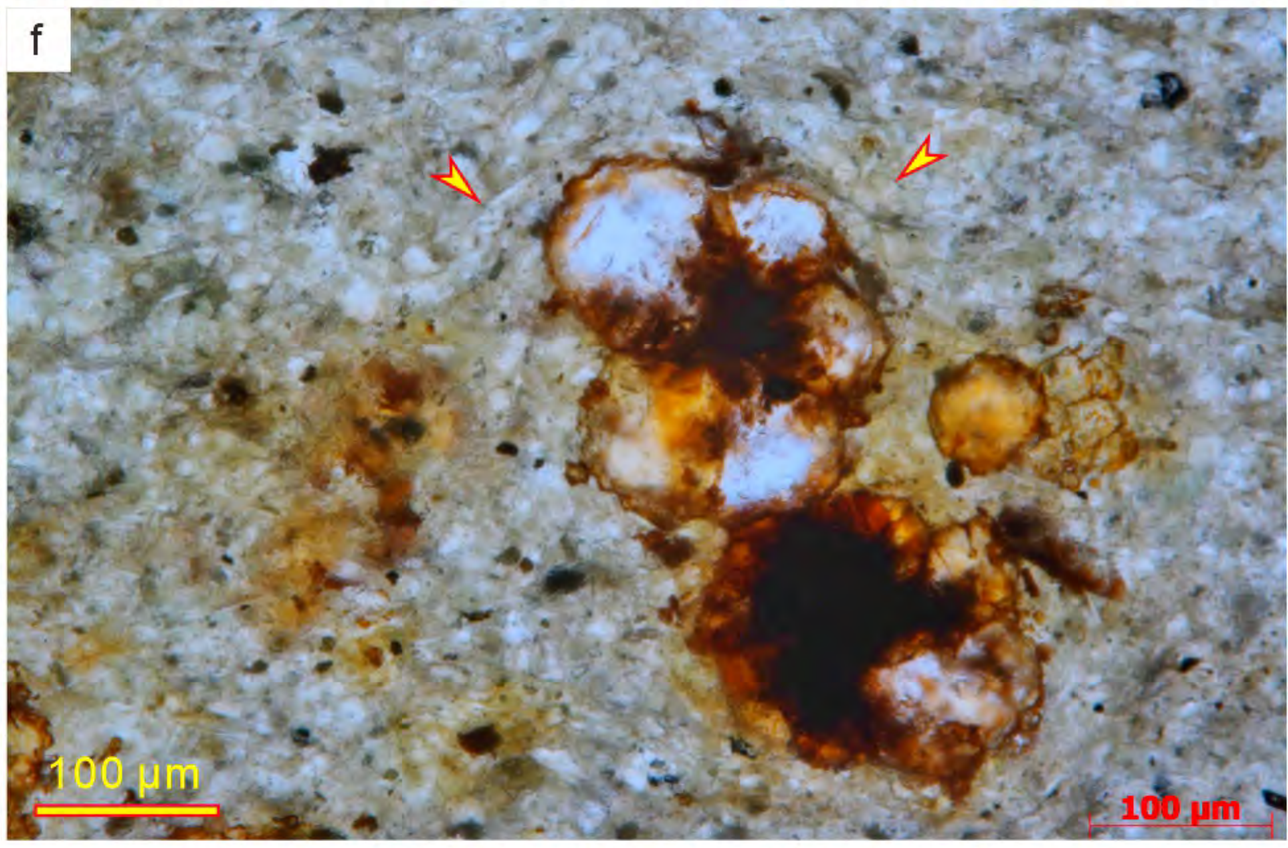
f
100 µm
100 µm

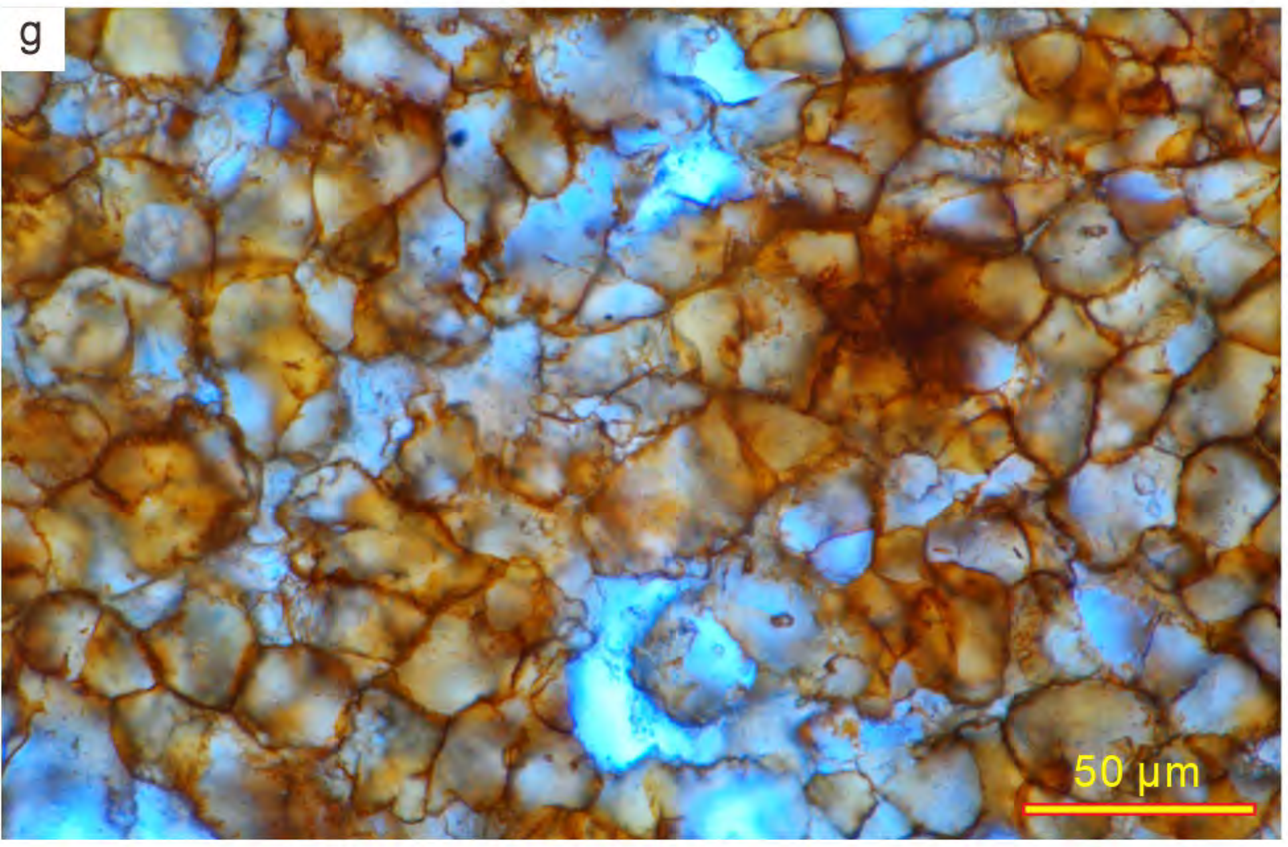
g
50 µm


h
1 mm

Figure 4

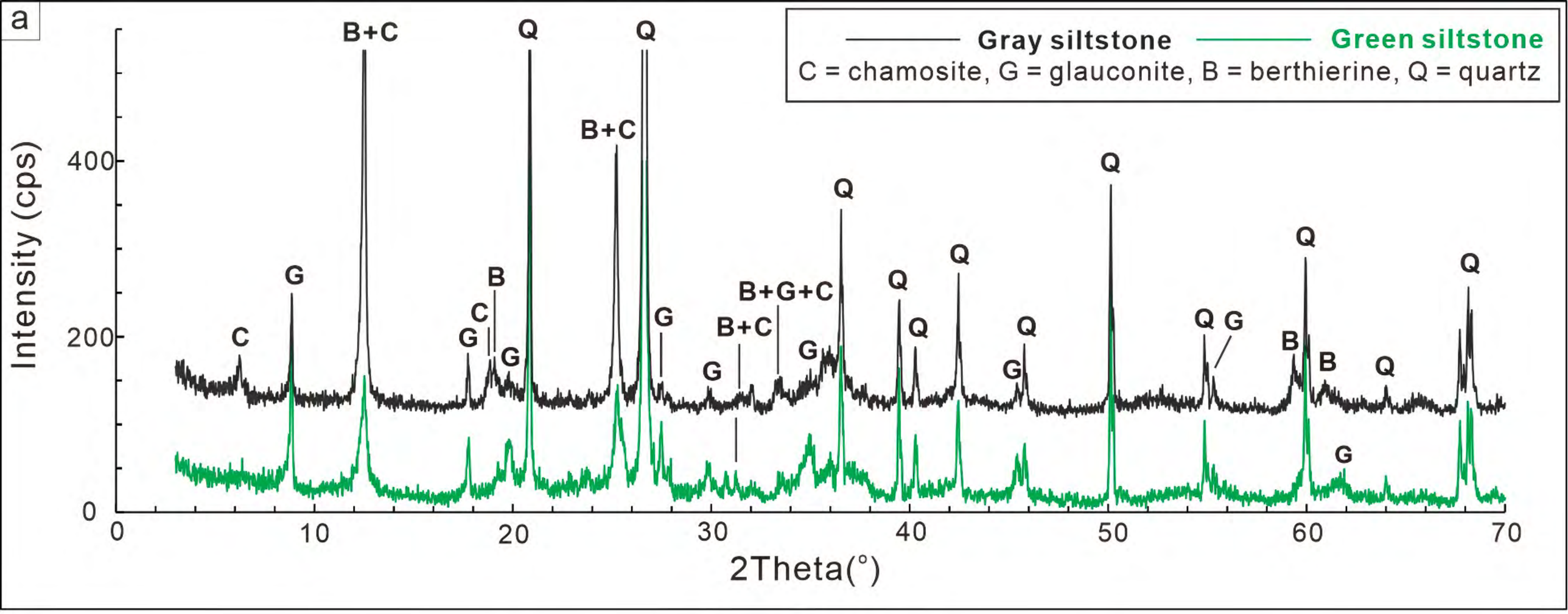
a
Gray siltstone
Green siltstone
C = chamosite, G = glauconite, B = berthierine, Q = quartz
Intensity (cps)
2Theta(°)
0
200
400
0
10
20
30
40
50
60
70
B+C
Q
B+C
Q
Q
Q
Q
Q
Q
Q
Q
Q
Q
B+G+C
B+C
C
G
G
C
B
G
G
G
G
G
G
G
G
B
B
Q
b
10 layers = 7.3 nm
Berthierine
5 nm
c
5 layers = 7.2 nm
6 layers = 4.4 nm
Berthierine + Chamosite
10 nm
d
9 layers = 9.3 nm
Glauconite
5 nm
e
1.0-nm-layers
0.7-nm-layers
Berthierine + Glauconite
5 nm

Figure 5

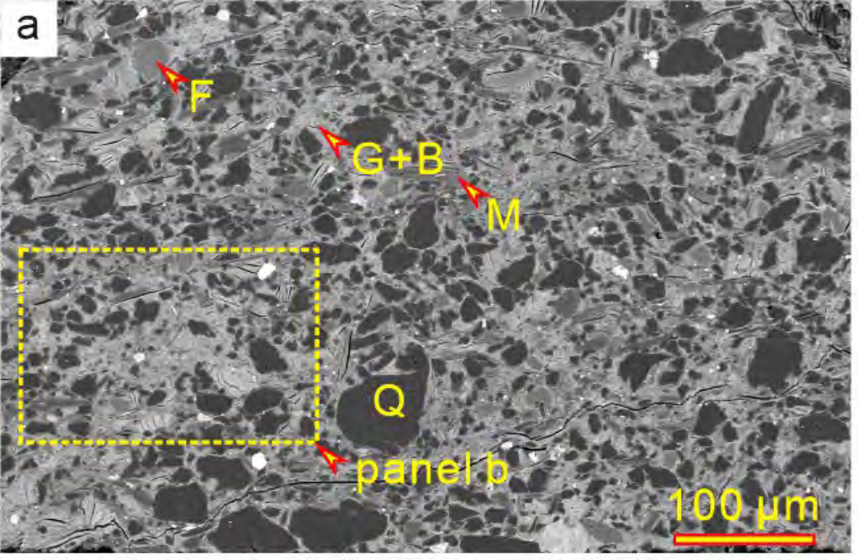
a
F
G+B
M
Q
panel b
100 μm

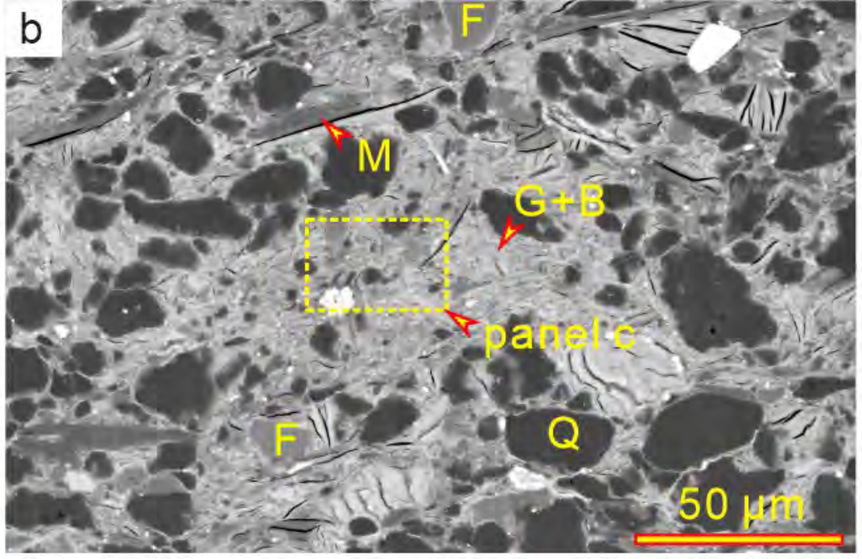
b
F
M
G+B
panel c
F
Q
50 μm

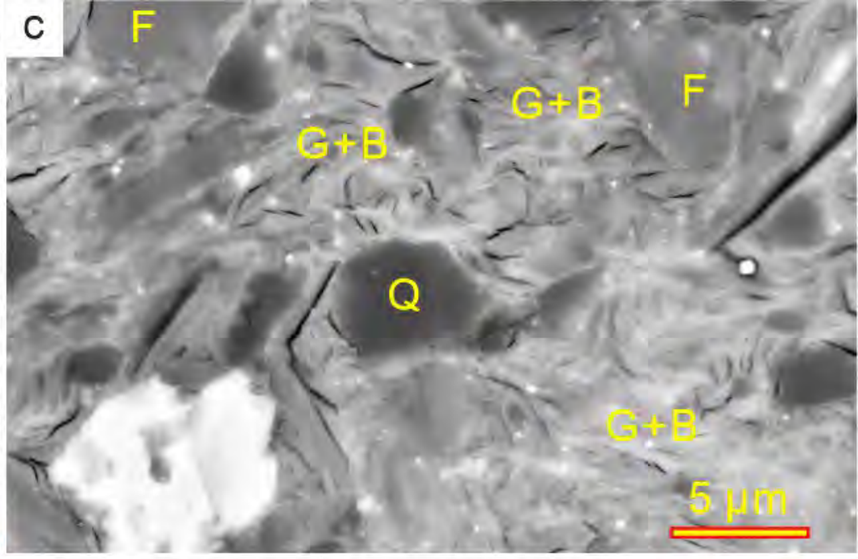
c
F
G+B
G+B
F
Q
G+B
5 μm

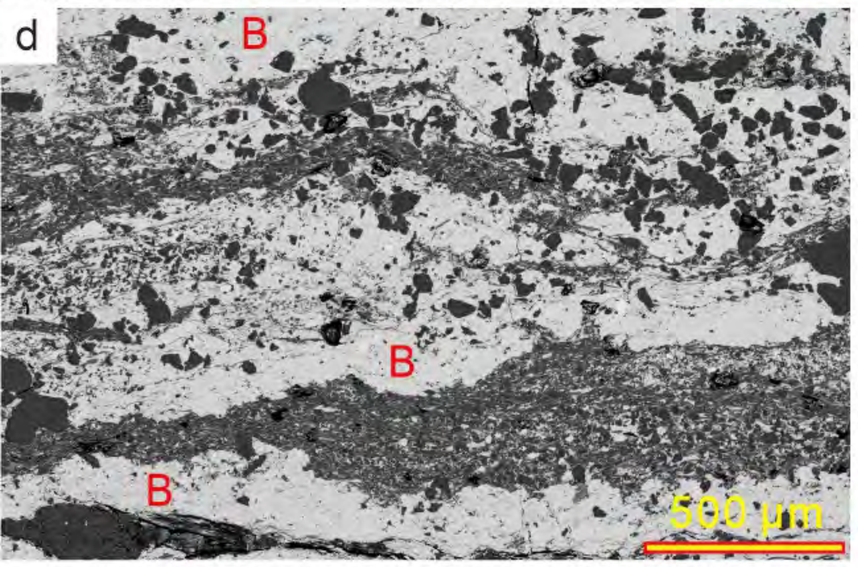
d
B
B
B
500 μm

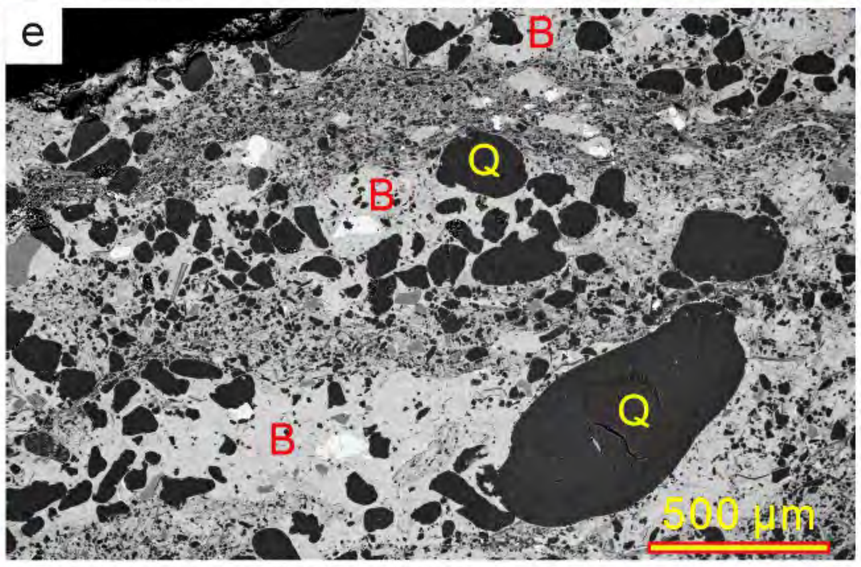
e
B
Q
B
B
Q
500 μm

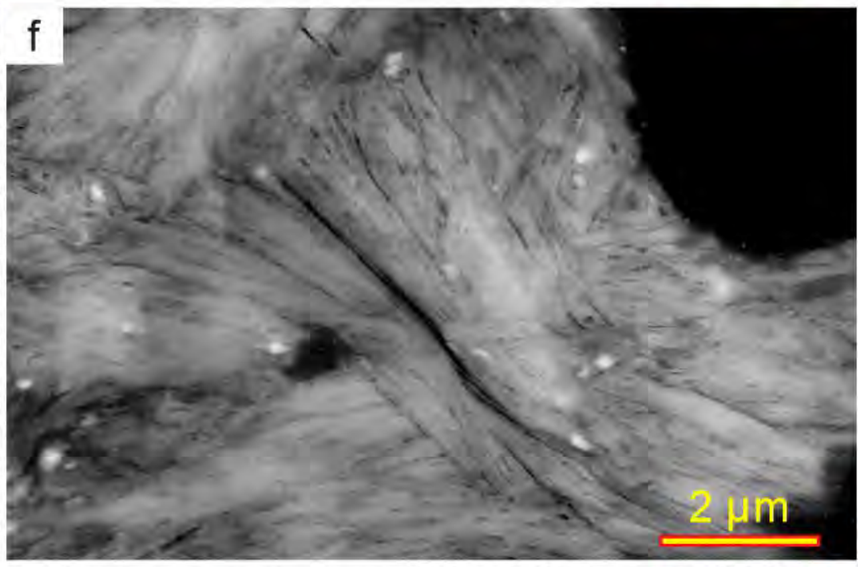
f
2 μm

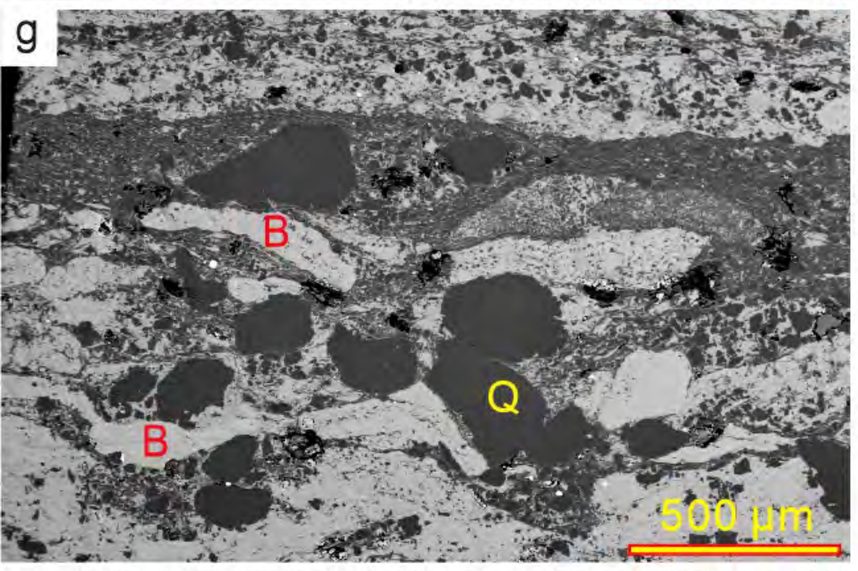
g
B
Q
B
500 μm

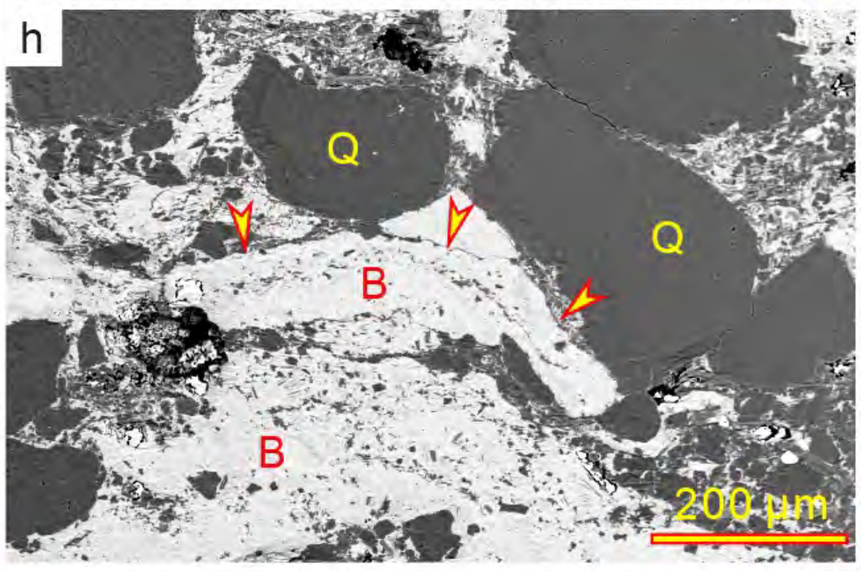
h
Q
Q
B
B
200 μm

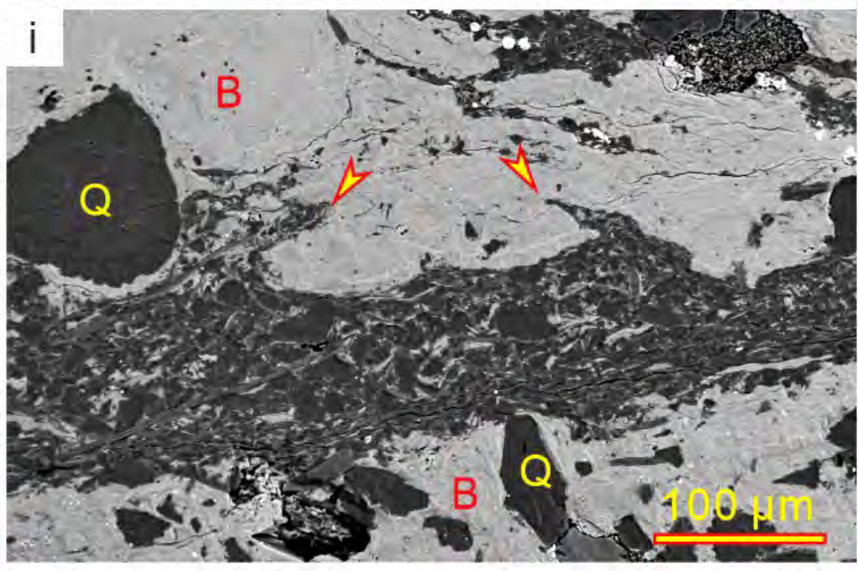
i
B
Q
B
Q
100 μm

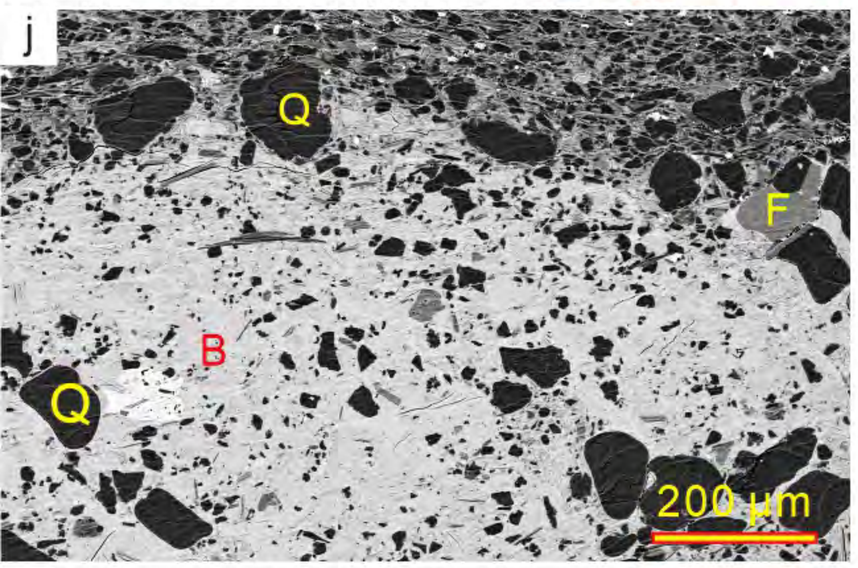
j
Q
F
B
Q
B
200 μm

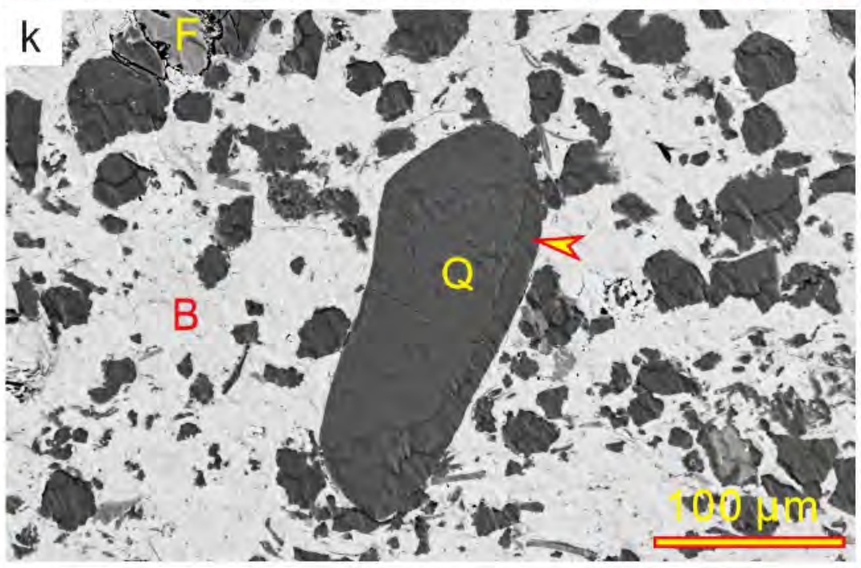
k
F
Q
B
100 μm

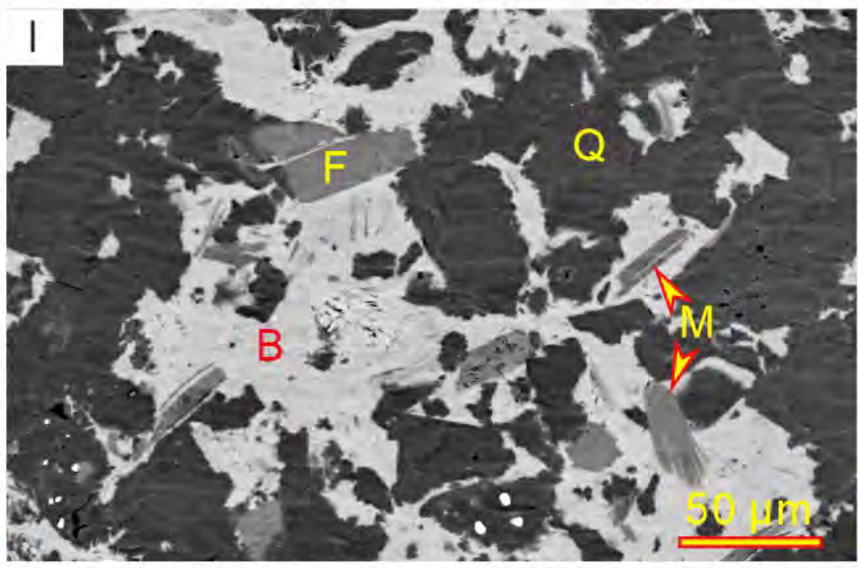
l
F
Q
M
B
50 μm


m
200 nm

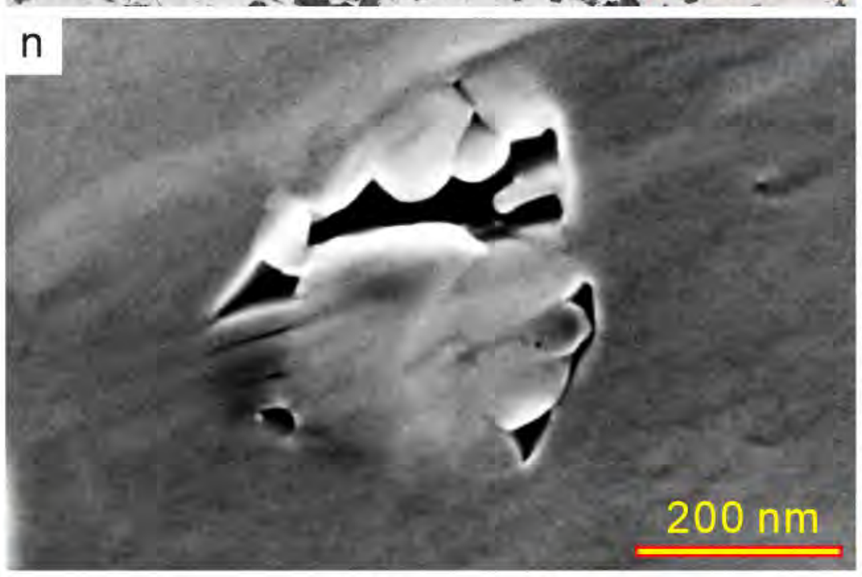
n
200 nm

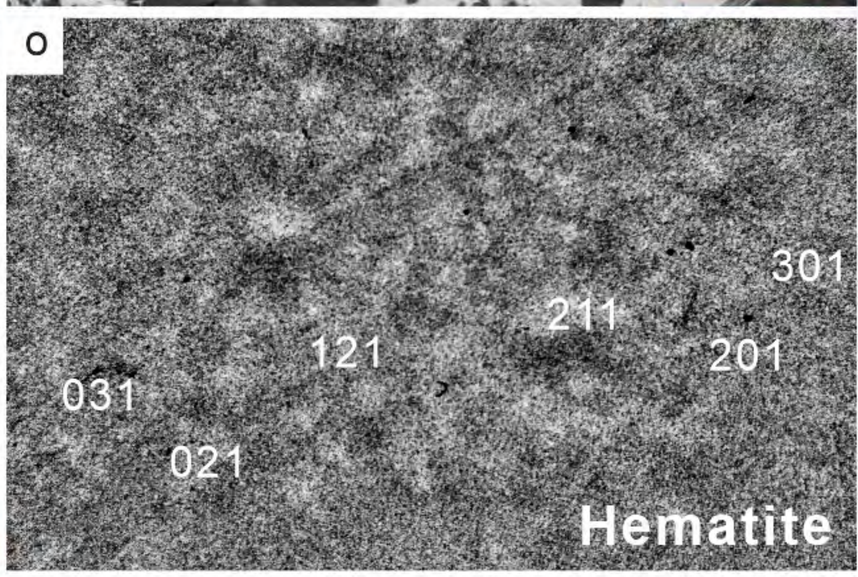
o
301
211
121
201
031
021
Hematite

Figure 6

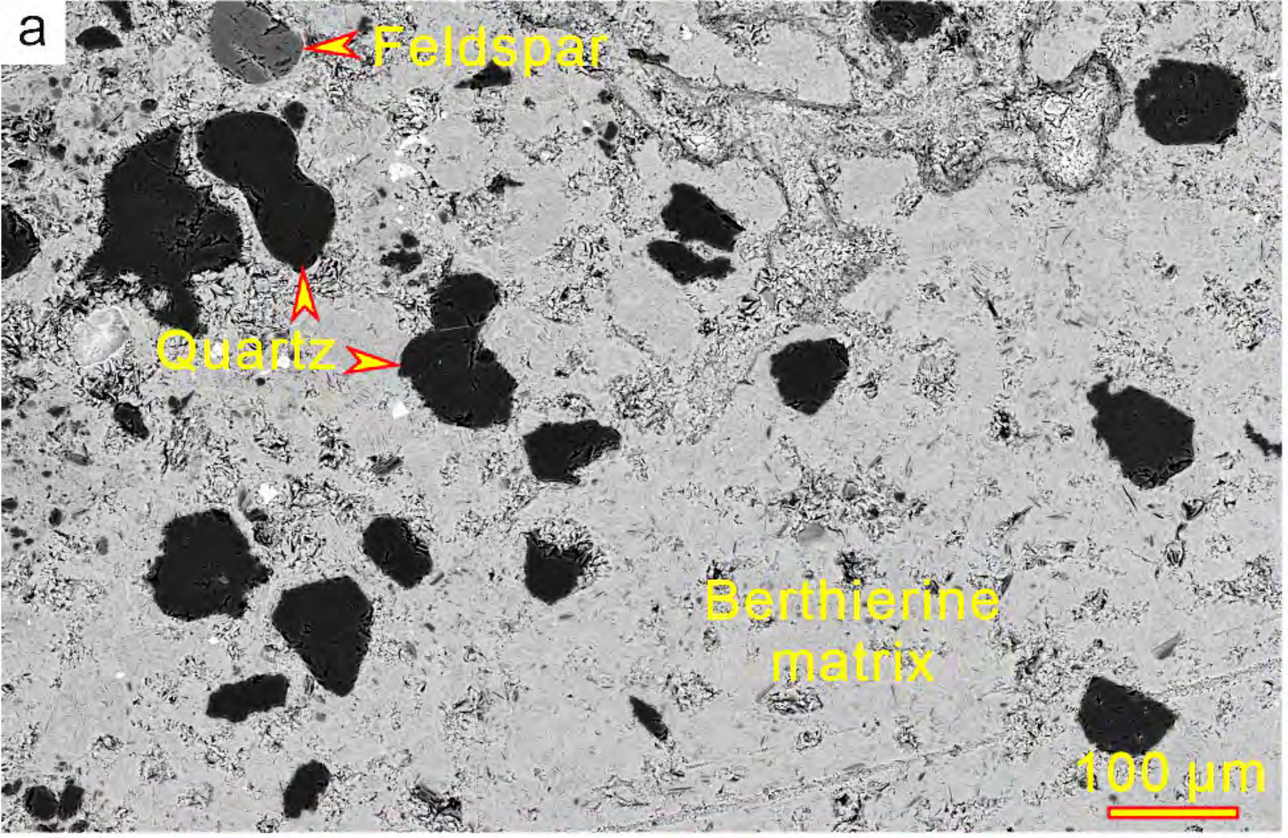
a
Feldspar
Quartz
Berthierine
matrix
100 µm

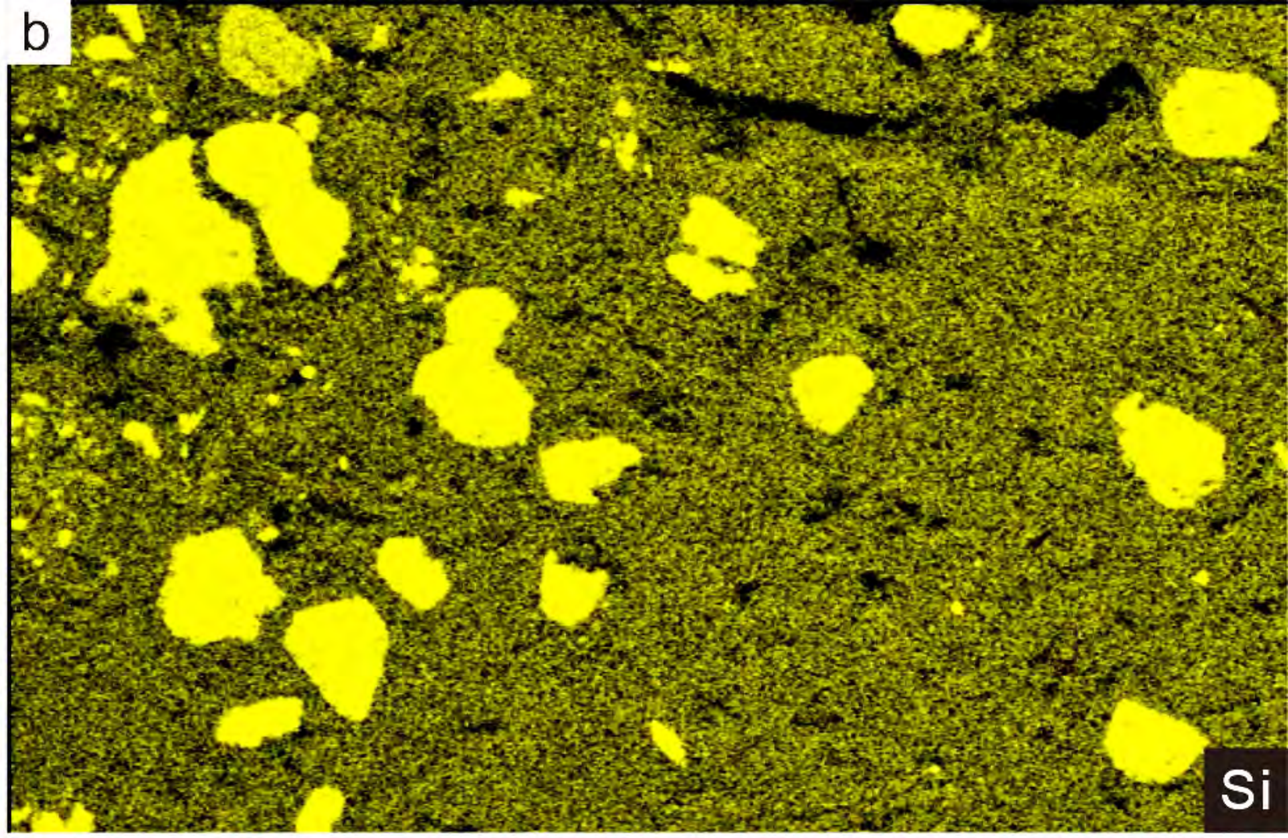
b
Si

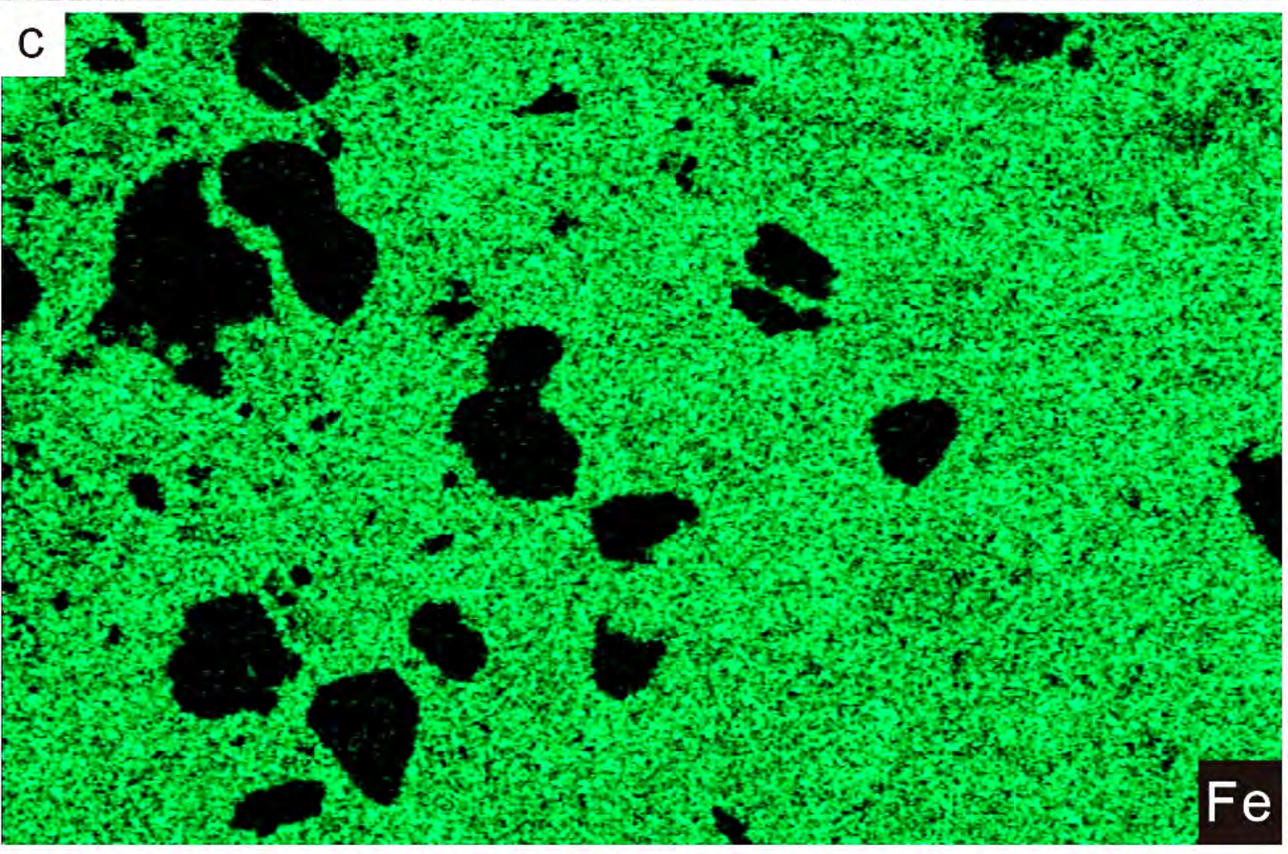
c
Fe

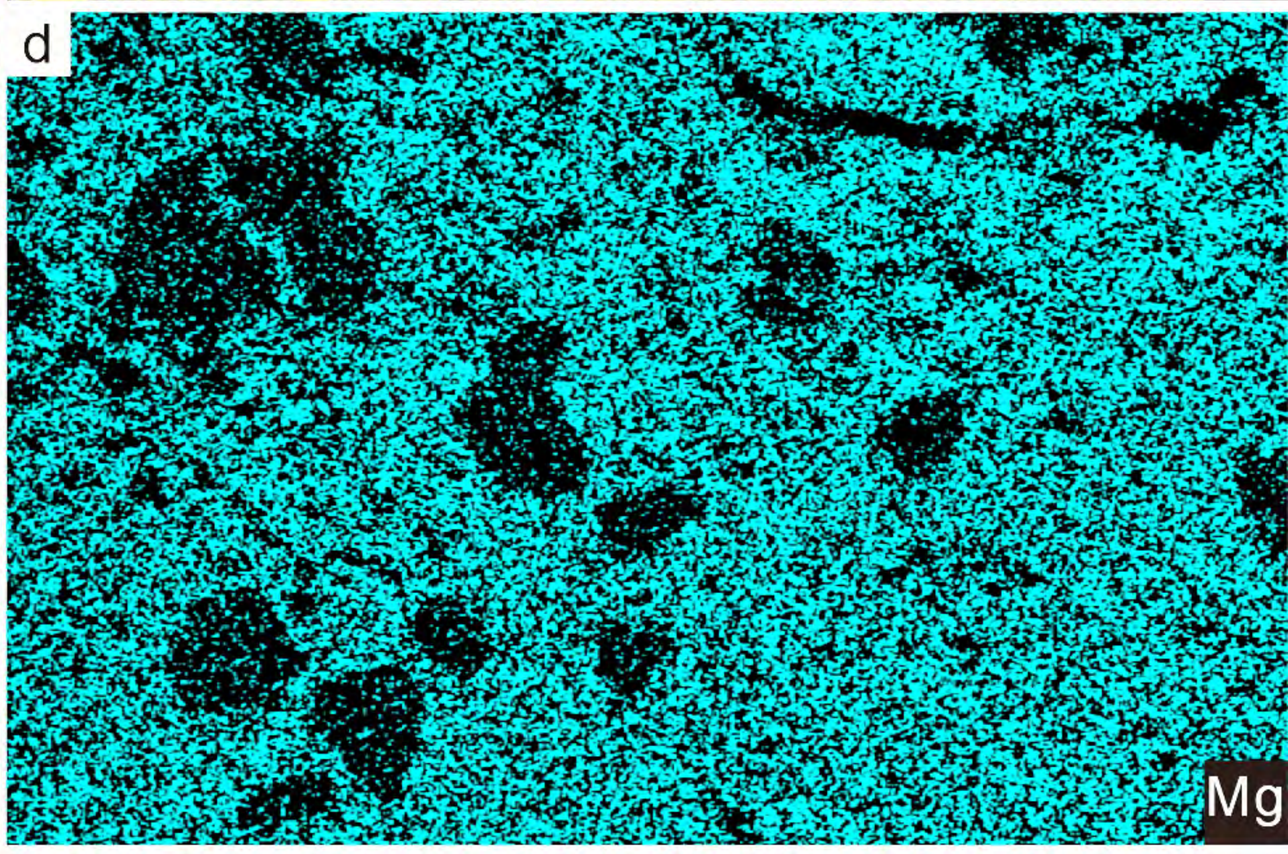
d
Mg

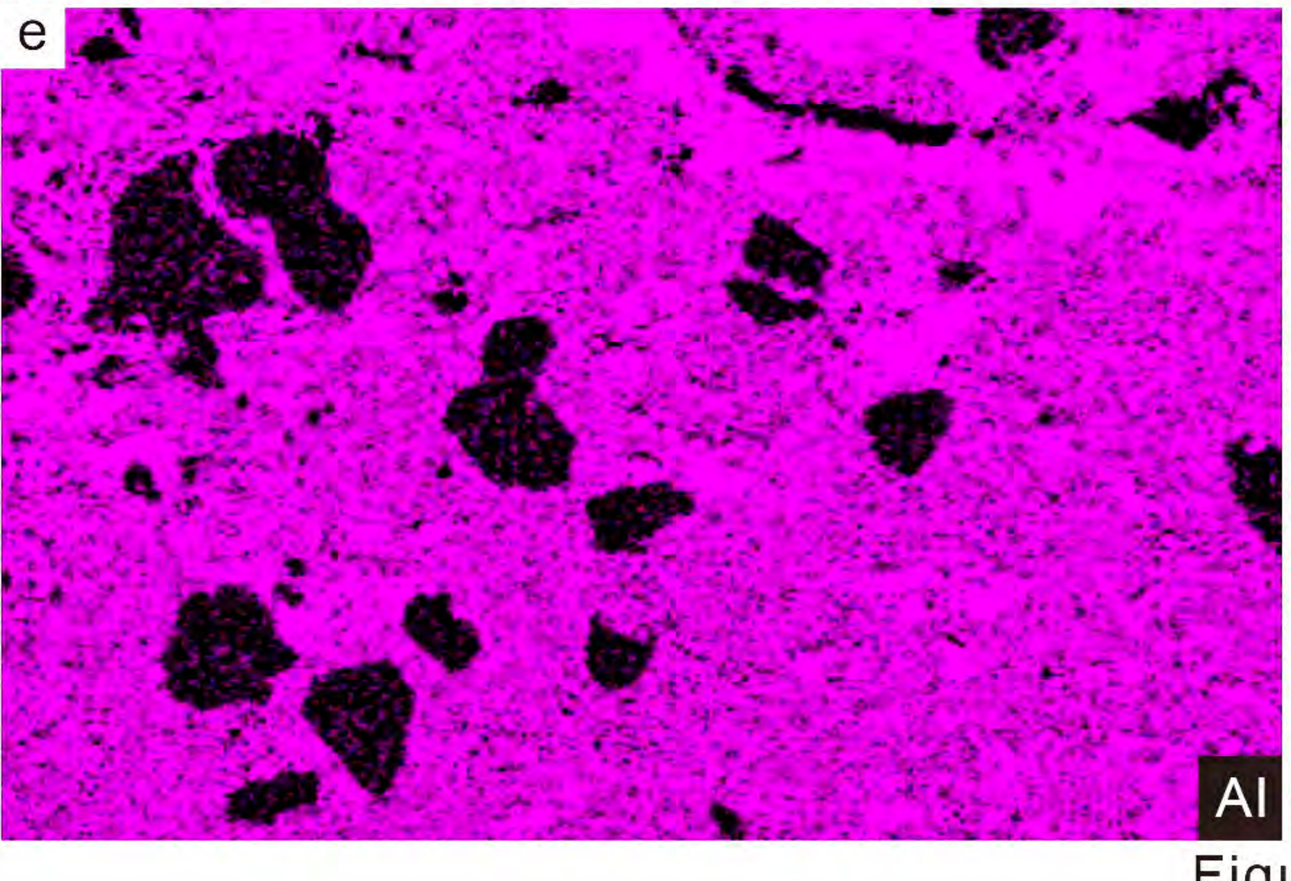
e
Al

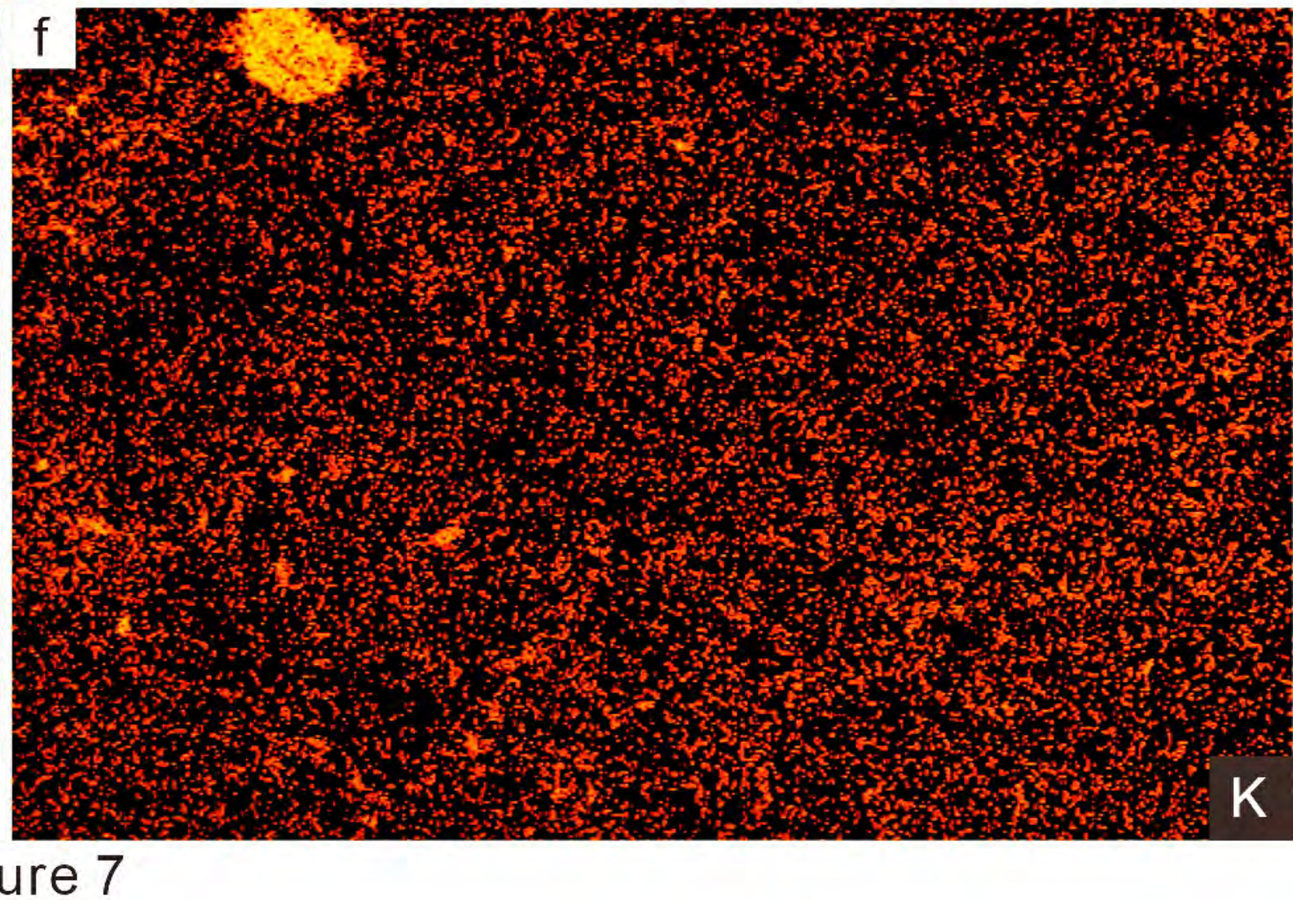
f
K

Figure 7

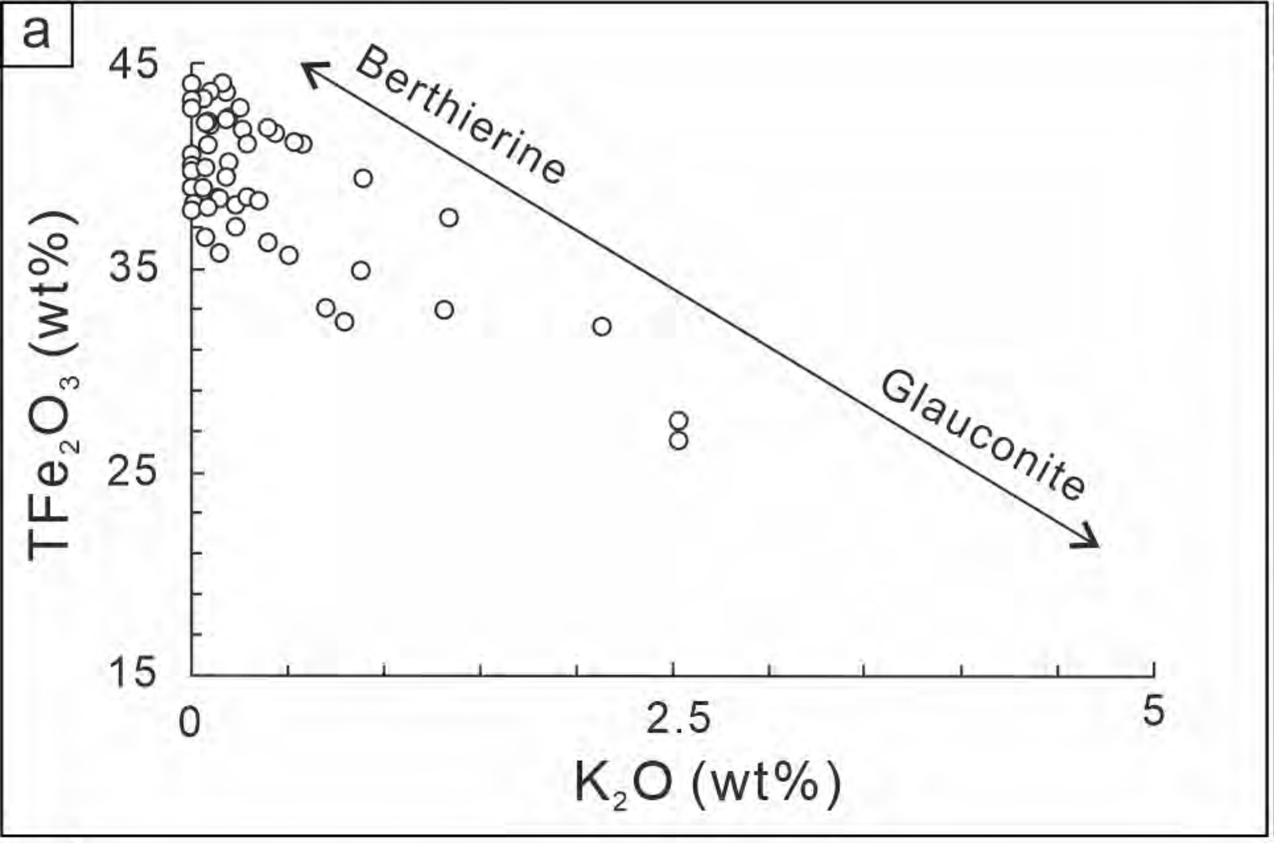
a
Berthierine
Glauconite
TFe2O3 (wt%)
K2O (wt%)
45
35
25
15
0
2.5
5

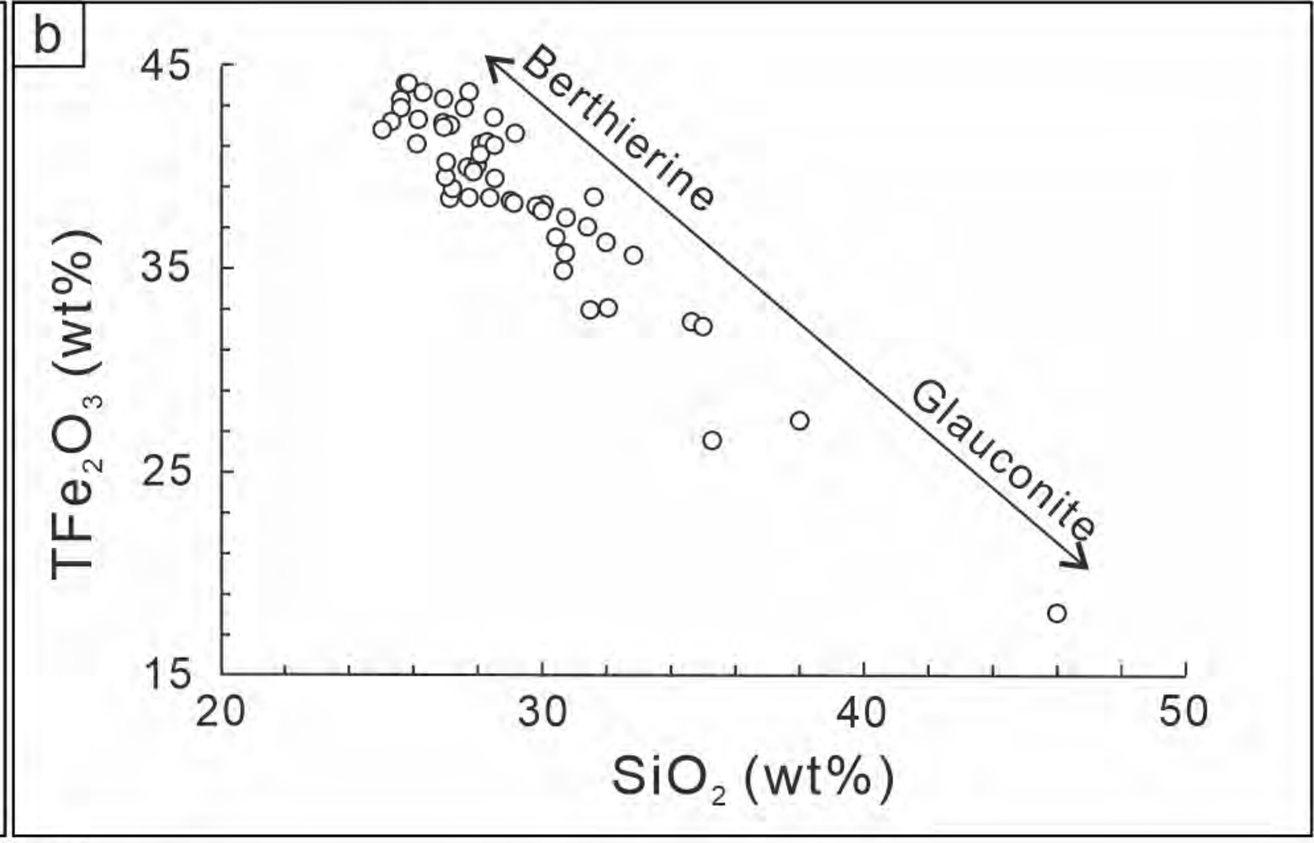
b
Berthierine
Glauconite
TFe2O3 (wt%)
SiO2 (wt%)
45
35
25
15
20
30
40
50

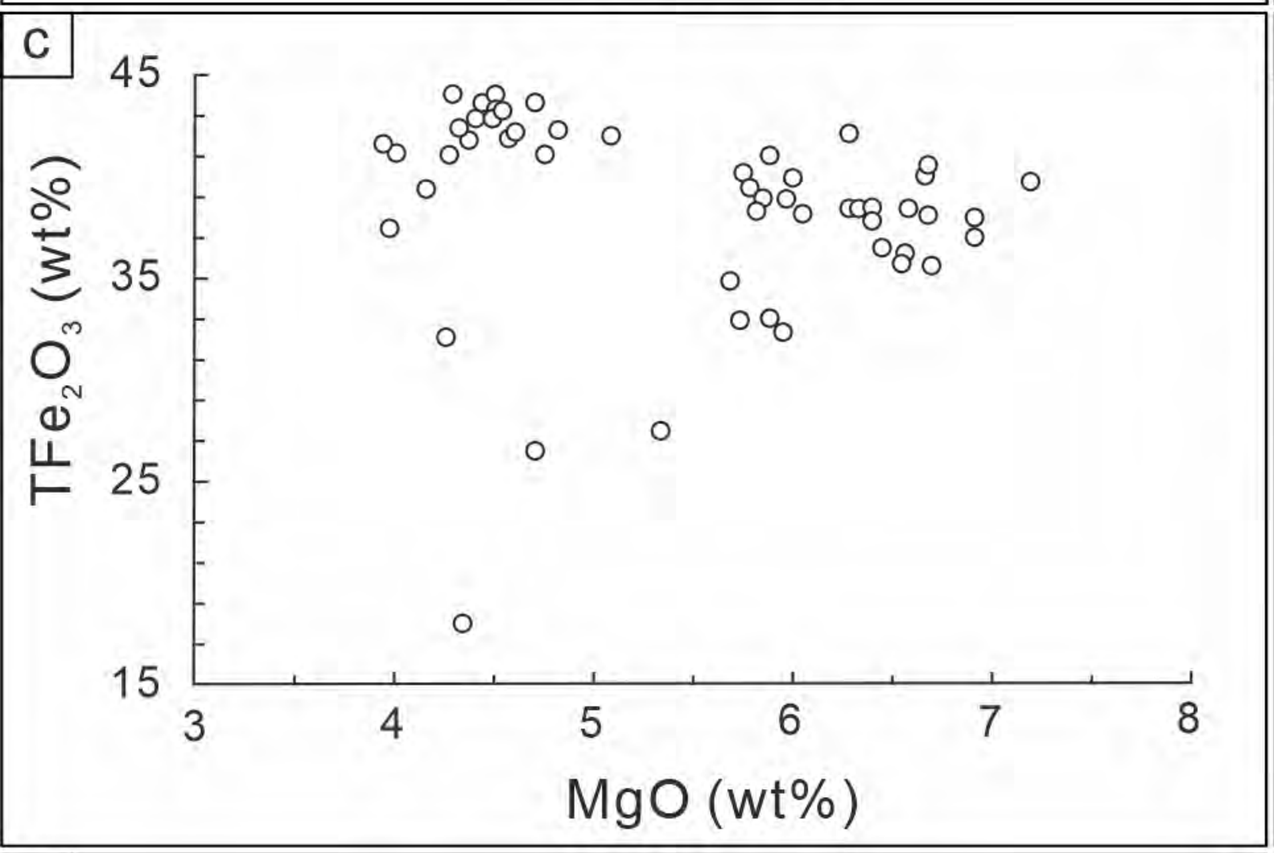
c
TFe2O3 (wt%)
MgO (wt%)
45
35
25
15
3
4
5
6
7
8

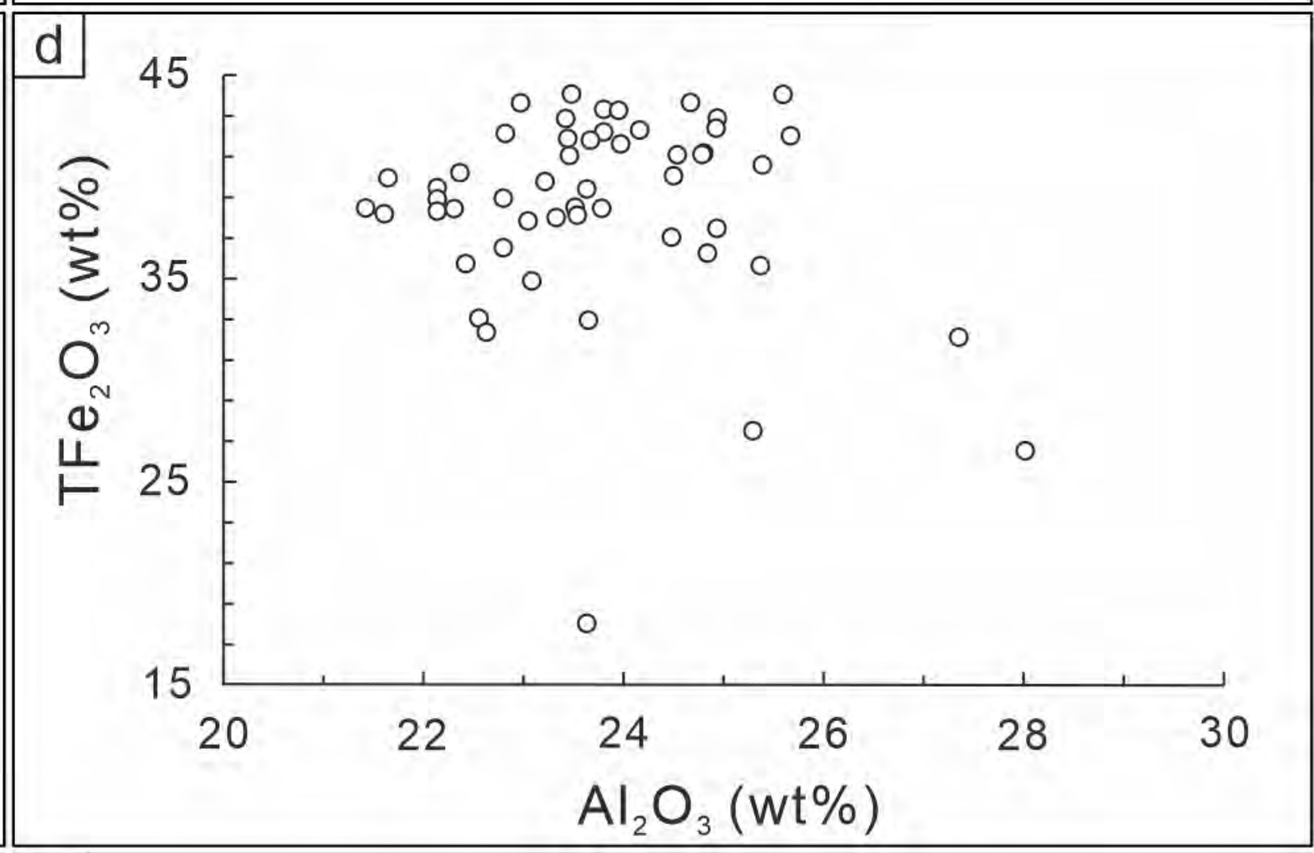
d
TFe2O3 (wt%)
Al2O3 (wt%)
45
35
25
15
20
22
24
26
28
30

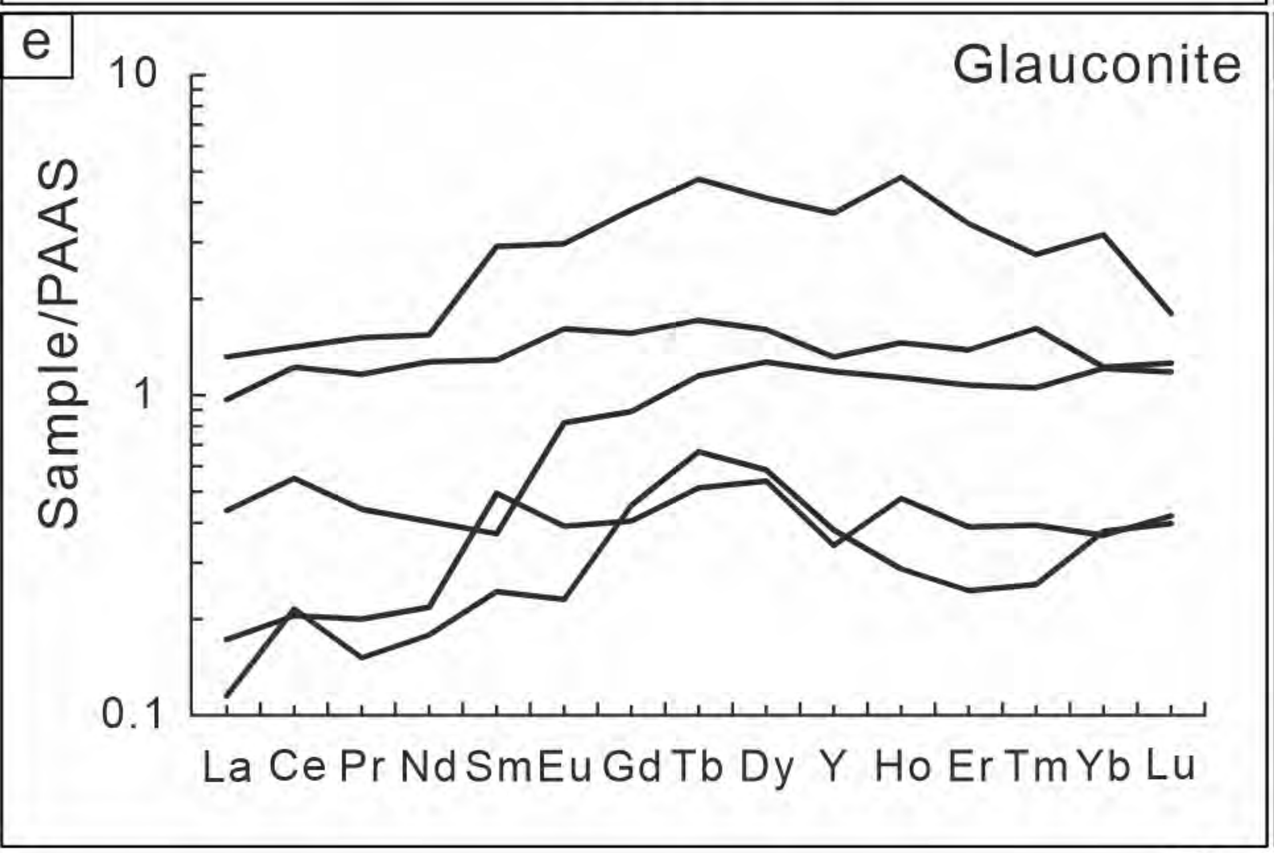
e
Glauconite
Sample/PAAS
10
1
0.1
La Ce Pr Nd Sm Eu Gd Tb Dy Y Ho Er Tm Yb Lu

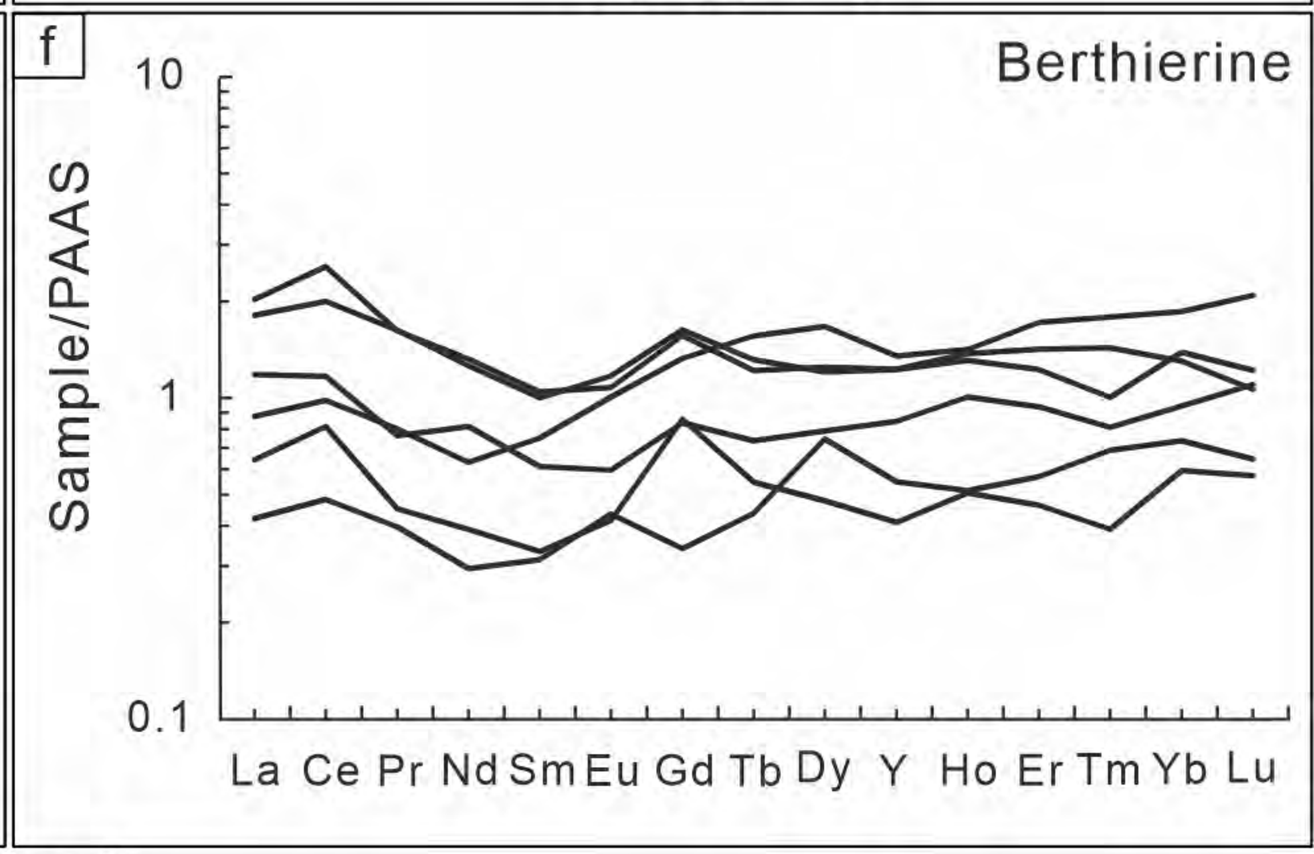
f
Berthierine
Sample/PAAS
10
1
0.1
La Ce Pr Nd Sm Eu Gd Tb Dy Y Ho Er Tm Yb Lu

Figure 8

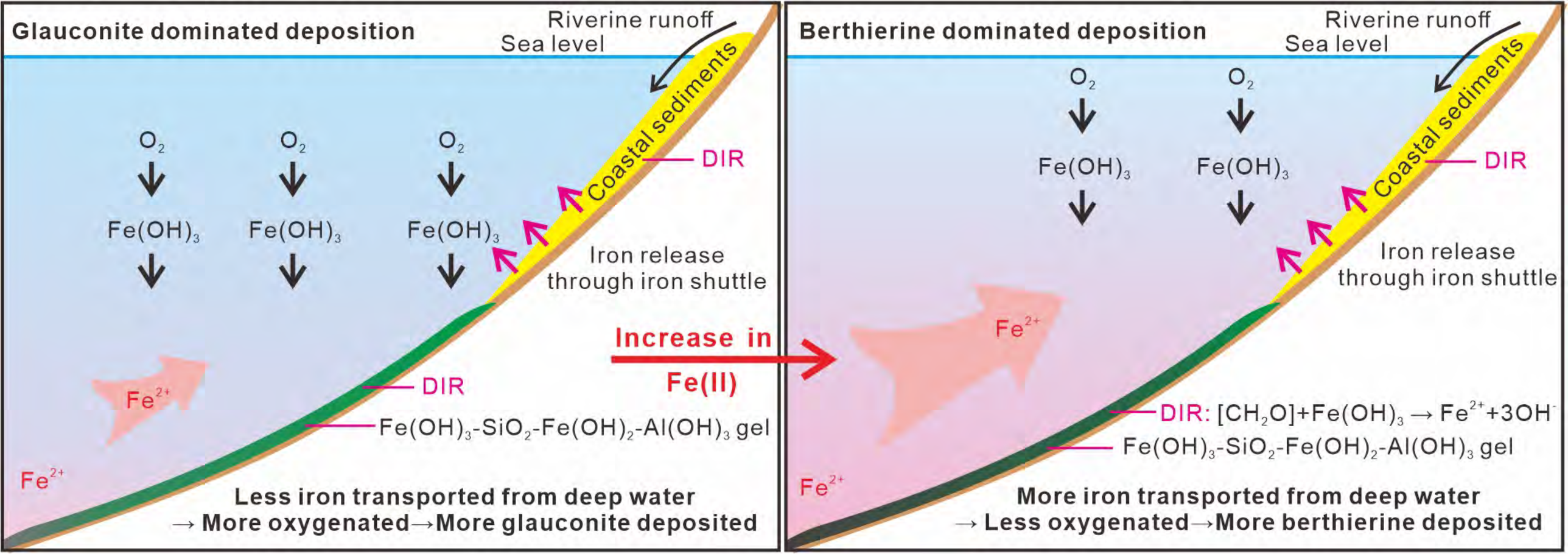
Glauconite dominated deposition
Riverine runoff
Sea level
Coastal sediments
DIR
O_2
$Fe(OH)_3$
Iron release
through iron shuttle
Increase in
Fe(II)
Fe^{2+}
DIR
$Fe(OH)_3$-SiO_2-$Fe(OH)_2$-$Al(OH)_3$ gel
Less iron transported from deep water
→ More oxygenated→More glauconite deposited
Berthierine dominated deposition
DIR: $[CH_2O]+Fe(OH)_3 \rightarrow Fe^{2+}+3OH^-$
More iron transported from deep water
→ Less oxygenated→More berthierine deposited

Figure 9